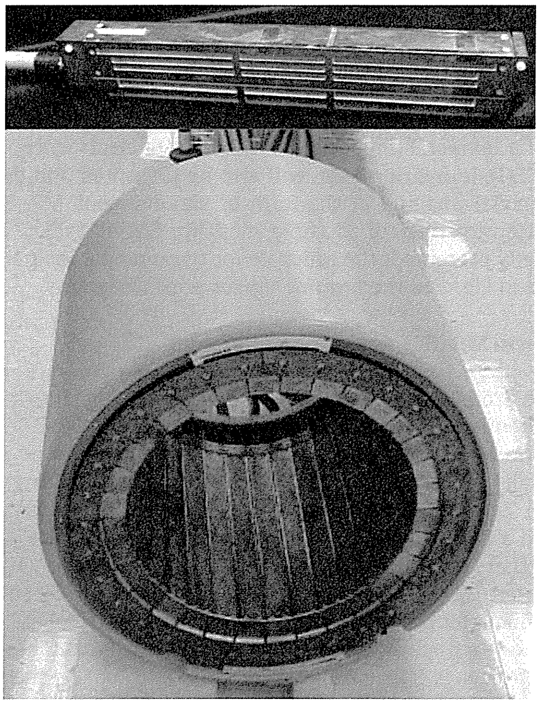

Fig. 2. A view of the interior of the BrainPET insert constructed as a ring of 32 individual cassettes. The BrainPET insert fits into the bore of the magnet of the MRI scanner and is positioned at the isocentre. Each cassette contains six detector modules in a row with a total length of 19.2 cm located towards the front end of the cylinder. Each cassette is individually radiofrequency shielded with a thin copper coating; this is to prevent RF noise generated by the PET electronics from disturbing the MRI signal and to reduce the influence of the MRI-related RF and gradient pulses on the PET system. The cassettes are connected to the MR filter plate by a 10 m, double-shielded cable.

human brain imaging with PET. The inner diameter of the BrainPET is 36 cm, this being the space for the MR head coil. For functional MRI, a custom-built mirror system is clipped onto the receive coil of the MR-head coil which allows for visual stimulus presentation. Hybrid MR–PET systems based on the above insert became available in late 2006 at 3 T and have enabled the acquisition of simultaneously acquired MR–PET data [10–12] some of which are presented below.

2.1. Multimodal imaging – hybrid MR–PET

As noted already, for the diagnostic evaluation of brain tumours, structural MRI is the routine approach. To overcome a challenging task for MRI, additional information from PET in cerebral gliomas, for example, may be very helpful in differentiating between tumour tissue, oedema and post-therapeutic changes in neighbouring tissue. Employing PET with amino acid tracers such as ^{18}F-Fluoroethyl-L-tyrosine (FET) or ^{11}C-L-methionine (MET) has been shown to be a powerful tool to resolve the diagnostic shortcomings of standard MRI examinations [1,13]. It should nevertheless be noted that although it does not form part of a standard examination, use of 1H-MRSI can also add valuable information [14]. Elevated concentrations of the cell membrane marker choline, for example, would support the presence of a tumour whereas a low choline peak in combination with high concentrations of the neuronal marker N-acetyl aspartate (NAA) would rather indicate an inflammatory process [15]. In brain tumours, especially in glioblastoma multiforme and anaplastic astrocytoma, the intracranial mass may be heterogeneous and consist of multiple compartments with differing degrees of malignancy. MRS is of help in the guidance of biopsies in inhomogeneous gliomas of WHO grade IV and also in low grade gliomas that show negative or nonspecific MET uptake with PET [16]. During therapeutic follow-up, amino acid PET and MRSI appear to be helpful in disentangling oedema, necrosis due to radiation therapy and the recurrence of tumour growth.

Diffusion tensor imaging (DTI) can contribute valuable diagnostic information regarding the involvement of white matter and fibre tracts [13,17,18]. Fibre tracking based on DTI data provides spatial information on the impairment of vital white matter fibre tracts, such as the pyramidal tract, by the tumour mass. Tumour infiltration or dislocation of such fibre tracts may considerably influence neurosurgical planning; a hybrid MR–PET examination that includes DTI is of considerable importance in this regard. Further, planning of neurosurgical intervention can be influenced by fMRI to identify eloquent brain areas close to the tumour and its resection zone. The joint findings from a hybrid MR–PET imaging session will impact considerably on the decision reached by the neurosurgeon regarding the necessary aggressiveness/extent of the neurosurgery, the approach to be taken e.g. anterior versus posterior, and the option of awake craniotomy with the possibility of direct cortical stimulation versus resection under general anaesthesia.

2.2. Clinical and neuroscientific applications of MR–PET at 3 T

Metabolic imaging for the differential diagnosis of brain tumours can benefit enormously from the intrinsic temporal and spatial co-registration of MR and PET data acquired in hybrid MR–PET systems [7–9]. Additionally, in the case of heterogeneous brain tumours or for differentiation between active tumour mass and scar tissue after radiation therapy, MR spectroscopy may help to cross-validate and/or extend the PET data. As already noted, the hybrid approach reduces measurement time and greatly aids patient compliance; some patients are simply unable to undergo two separate scans. The feasibility of combining anatomical information from an MP-RAGE acquisition, metabolite-specific information from MR spectroscopy, and FET-PET in the investigation of brain tumours in humans using a hybrid MR–PET scanner was recently demonstrated [12].

MR–PET data from a representative patient from our study comprising a collective of over 50 tumour patients are shown in Fig. 3. The top row of Fig. 3 shows the diffusion parameter FA superimposed on a T_1-weighed MP-RAGE dataset; the crosshairs mark the location of the tumour as determined from FET-PET which shows almost no enhanced tracer uptake in the regions depicted by MRI that are hypointense in the MP-RAGE acquisition. The bottom row of Fig. 3 shows the location of the tumour as well as activation of default mode networks from resting-state fMRI.

MR spectroscopy may also provide metabolic information in addition to FET-PET and detect regional abnormalities of choline, creatine and myo-inositol concentration in large homogeneous low grade gliomas (Fig. 4). This may be an early sign of malignant transformation of a low grade glioma.

These measurements have shown that the acquisition of multimodal MR–PET data sets can contribute significantly to the differential diagnosis of pathological brain lesions. Based on the MR images, the pathological region can be further evaluated by FET-PET and MR-spectroscopy. In cross validation, both image modalities show that the lesion depicted in the MR images (Fig. 4) could be due to inflammation rather than being a malignant tumour thereby illustrating the benefits of multi-modal imaging.

Localisation of functional areas in presurgical fMRI is also an application that benefits from hybrid MR–PET. The appropriate choice of therapy for a brain tumour mandates that the diagnosis encompass the anatomical location, size, spread to different anatomical compartments, and evaluation of tumour malignancy.

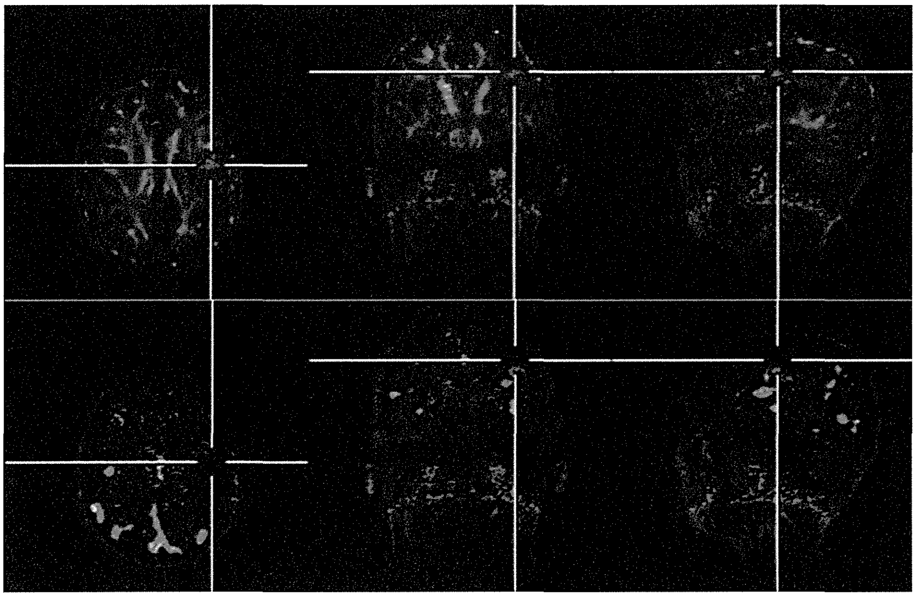

Fig. 3. Images acquired on a hybrid MR–PET scanner comprising a 3 T MAGNETOM Tim-Trio MR and a BrainPET insert. Top: the diffusion parameter, FA, superimposed on a T_1-weigthed MP-RAGE dataset; the crosshairs mark the location of the tumour as determined from FET-PET which shows almost no enhanced tracer uptake in the regions depicted by MRI that are hypointensive in the MP-RAGE acquisition. Bottom: the location of the tumour as well as activation of default mode networks from resting-state fMRI are depicted. PET images acquired within 45 min scanning time after injection of 200 MBq of the amino acid O-(2-[18F]Fluorethyl)-L-Tyrosin (FET).

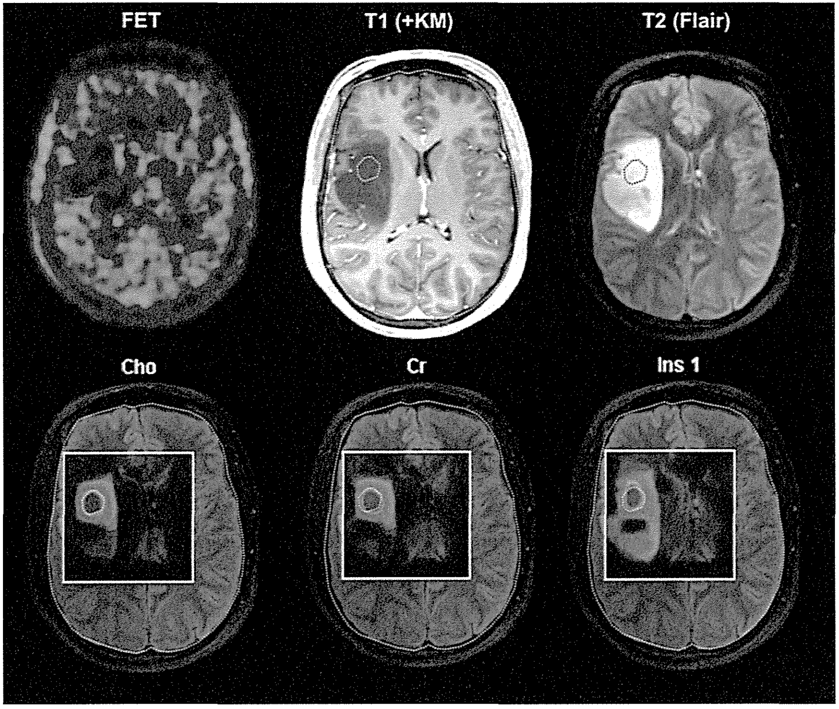

Fig. 4. Patient with a large astrocytoma WHO Grade II in the right temporal lobe. FET PET (upper left) demonstrates low amino acid uptake in the tumour suggesting a favourable prognosis. MRS (chemical shift imaging) shows a regional abnormality in the tumor with increased concentration of choline, creatine and myo-inositol (lower row) which may be an early sign of malignant progression.

Moreover, in contrast to common non-brain tumours, therapy options for these tumours are partially set by their proximity to areas of major brain function, such as motor function, somatosensory, and language, the exact locations of which are dependent upon the individual. Simultaneous MR–PET measurements with optimum temporal and spatial co-registration open up an opportunity to measure the size and the location of the tumour, in relation to regions involving essential brain functions, based on high-resolution MRI and fMRI. Tracer uptake rate, as shown in the PET images, also facilitates insights into the pathophysiology of the tumour, in particular into its degree of malignancy. In Fig. 5, an example of speech area localisation is shown.

The speech area was localised by employing standard, BOLD-based fMRI during stimulation with a speech localisation paradigm comprising a block design of 4 × 36 s stimulation periods nested into five resting periods of 18 s duration each [19]. Briefly, in order

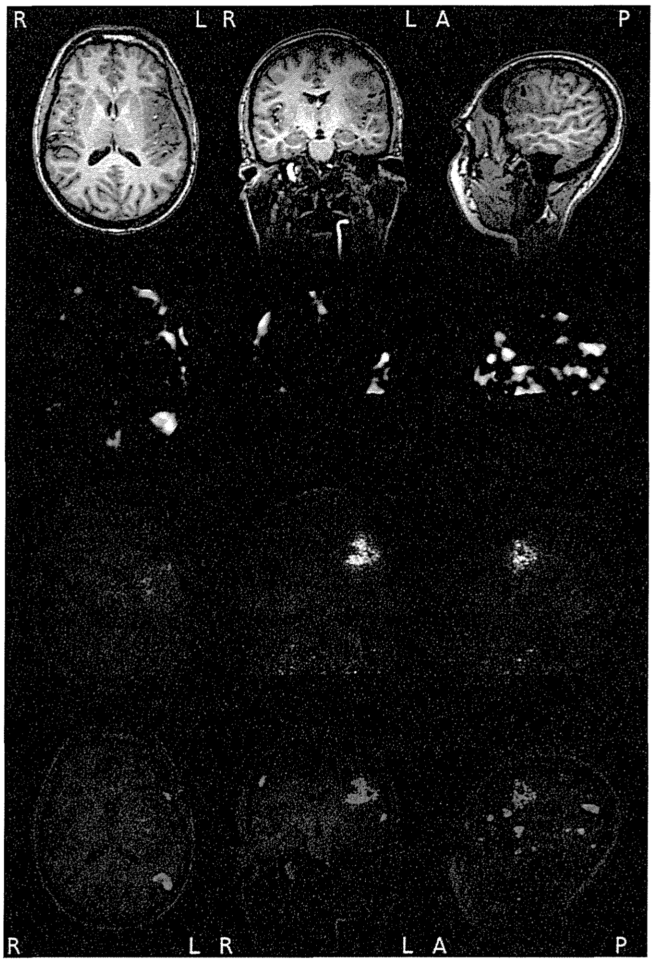

Fig. 5. Data from a 38-year old women suffering from a left, fronto-temporal oligoastrocytoma. Top row: The MRI data from a T_1-weighted MPRAGE sequence (1 mm isotropic resolution) shows an oligoastrocytoma fronto-temporal on the left side. 2nd row: The language localisation paradigm yields a strong BOLD signal at the position of the speech associated areas. 3rd row: The FET-PET reveals a tracer enhancement at the location of the tumour (200 MBq, 50 min scanning time). Bottom row: Fusion of the three imaging modalities; this transverse slice (bottom, left) shows a bright occipito-temporal area of fMRI activation which corresponds to the activation of the Wernicke speech area far from the tumour. On the same slice, it can be seen that the tumour is beginning to infiltrate the Broca language area at its fronto-lateral border. This additional information can guide decisions regarding the appropriate therapy for this patient.

to fully stimulate the complex speech area, the paradigm comprises two parts, word and sentence generation. For word generation, generic terms were presented on a display and the patient was required to find matching examples. In the sentence generation paradigm, simple pictures were presented which had to be transferred into sentences.

The data from a 38-year old woman suffering from a left, fronto-temporal oligoastrocytoma are shown in Fig. 5. The transverse slice (bottom, left) shows a bright occipito-temporal area of fMRI activation which corresponds to the activation of the Wernicke speech area far from the tumour. On the same slice, it can be seen that the tumour is beginning to infiltrate the Broca language area at its fronto-lateral border. This additional information can guide decisions regarding the appropriate therapy for this patient.

2.3. Multimodal imaging – simultaneous fMRI–EEG at 3 T

Functional MRI, relying on the measurement of the BOLD effect, has successfully been used to probe functional aspects of the brain including the assessment of different sensory, cognitive, emotional and social tasks [20,21]. However, the main drawback of fMRI is the fact that the BOLD effect is an indirect measure of brain function with a low temporal resolution due to the delayed haemodynamic response. This restriction can be overcome by the simultaneous measurement of fMRI and electrophysiology [22–24]. Electrophysiological measures (e.g. EMG and EEG) assess neuronal function on a millisecond timescale, thus providing the temporal resolution missing in fMRI. fMRI on the other hand provides excellent spatial resolution that is lacking in EEG data. Combining fMRI and EEG measures thus allows one to probe a scientific question in one individual with two modalities spanning a high spatial resolution (MRI/fMRI) and a very fine temporal resolution (EEG) at the same time under exactly the same physiological, psychological and technical conditions. Neuroscientific studies involving paradigms where a parallel paradigm version might evoke confounding factors, studies using pharmacological challenges or paradigms relying on novelty effects also profit from a simultaneous approach due to the elimination of order and learning effects. The simultaneous approach is also important for the investigation of the "resting state" [25,26]. It allows for the analysis of the underlying neuronal phenomena of oscillation amplitude fluctuations in the EEG data which reflect functional states and can be used for the definition of such states. Furthermore, these have been shown to affect behaviour when occurring in a task context. Simultaneous EEG–fMRI has proved to be particularly useful in studies of sleep and epilepsy where significant events, such as epileptic spikes or sleep onset, can be identified in the EEG and used for appropriate analysis of the fMRI data [27]. Without the high temporal resolution EEG data for event identification, effective analysis of the fMRI data would not be possible.

Simultaneously acquired EEG/fMRI data are also a prerequisite for a single trial analysis approach to integrating EEG and fMRI data. Based on the single trial e.g. prepulse–pulse inhibition (PPI) of the startle reflex or P300 latency or amplitude, an electromyography (EMG) or EEG-informed fMRI analysis becomes feasible [22,28–30]. In a classical approach to EEG and fMRI data analysis, averaging of trials is usually performed meaning that the trial-to-trial evoked response variability is averaged out [31]. Fluctuations in evoked responses such as the P300 as well as spontaneous activity changes e.g. during "resting state" investigations mirror fluctuations of an internal and predictive contextual representation [32], thus making this variability meaningful and these data could broaden the functional understanding of neuronal networks.

The examples above show how both modalities complement each other effectively. However, the simultaneous acquisition of fMRI and EEG data is technically challenging and comes at a price with regard to data quality. From a technical perspective recording EEG during fMRI requires an MR-compatible EEG-system (which are commercially available) and great care during recording inside the scanner to ensure safety of the volunteers and acceptable data quality [22,29]. In terms of quality, EEG data acquired simultaneously with fMRI data suffer two types of artefacts: (a) the so-called cardioballistic artefact or pulse related artefact caused by slight pulse-induced head motion and by pulsation of scalp vessels within the magnetic field, and (b) the gradient artefact caused by switching of the gradients during the EPI sequence favoured for fMRI [33]. As shown in Fig. 6, both artefacts can be successfully removed from the EEG by different methods such as Artefact Average Template Subtraction [34], Optimal Basis Set [35] or Independent Component Analysis [36,37]. As MRI moves towards ultra-high field imaging the question of whether the simultaneous approach would still be feasible needs to be addressed. EEG data acquired at 7 T [36] and 9.4 T [38] show that the cardiac-related pulse artefact increases linearly with field strength and is more challenging to remove from the data, but that in principle EEG

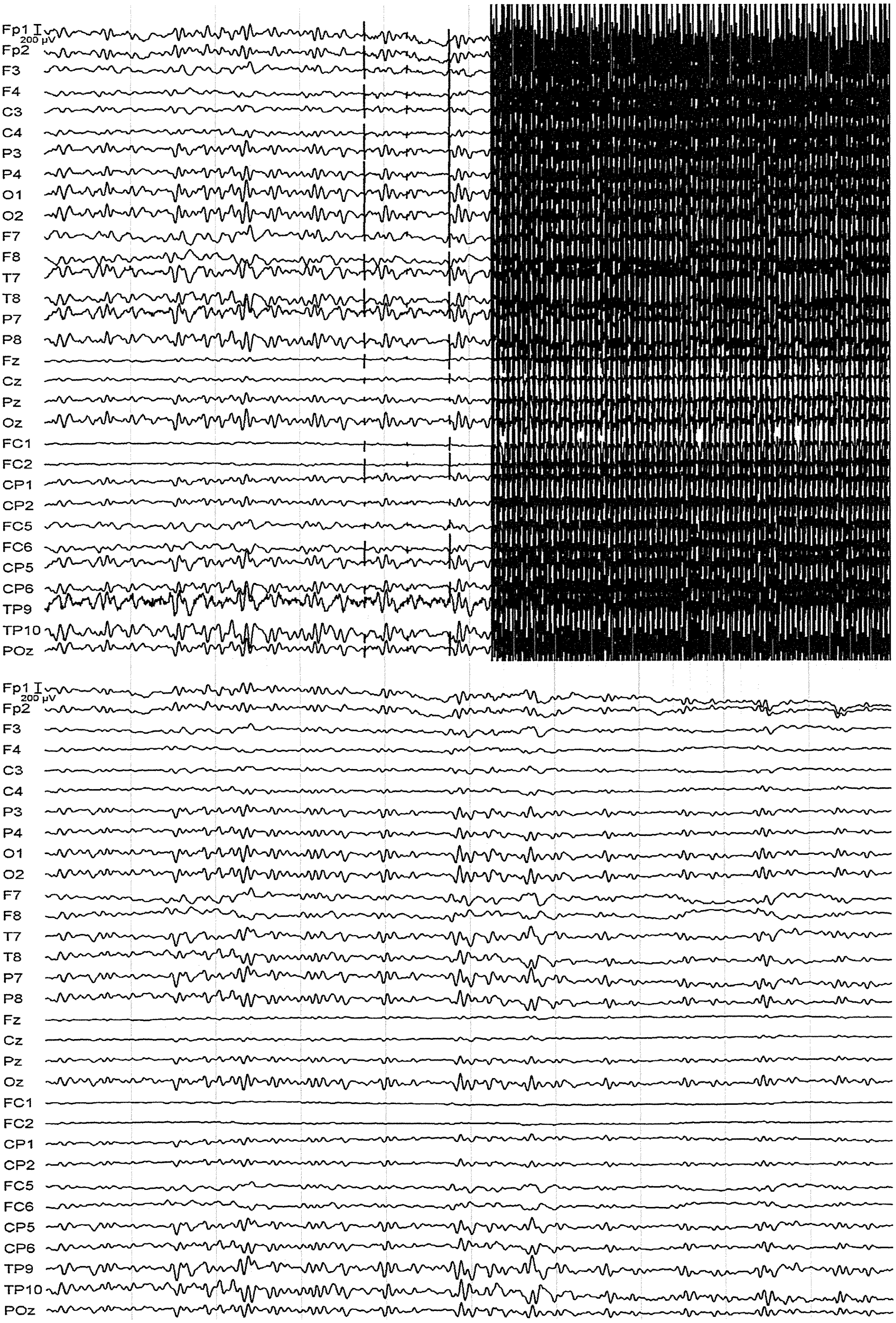

Fig. 6. The upper part of the figure shows uncorrected EEG-data acquired in a 3 T MR scanner: The left side shows data prior to the start of the MRI acquisition, distortion due to the cardio-ballistic artefact in the static field can be seen. The right side of the image shows the gradient artefact. The lower part of the figure shows the same section of data that has been corrected for cardio-ballistic artefact and gradient artefact.

and event-related potential (ERP) data recording is feasible [38]. An example of the variation in the ECG wave and the cardiac-related pulse artefact in the EEG channels over different field strengths, up to 9.4 T, recorded in a 23-year old healthy volunteer is shown in Figs. 7 and 8.

2.4. Simultaneous MR–PET–EEG

Even though MRI and EEG complement each other with regard to their spatial and temporal resolution (see Fig. 1), the underlying molecular basis of a probed task or resting state analysis is not accessible using these methods. As already noted, observing the molecular basis at transmitter system level is the domain of PET; it is the gold standard for the investigation of brain metabolism via 18-FDG-PET, the striatal D2-receptors via 11C-raclopride or the GABAergic system via 11C-flumazenil, for example. Though PET yields highly specific information at the molecular level, its spatial resolution is low and it comes with the disadvantage of some radiation exposure for the volunteers/patients. Thus, neuroscientific hypotheses have to be probed in a very efficient manner when investigating healthy subjects. The new technological development of hybrid MR–PET scanners fosters this approach. Explicitly, a comprehensive imaging protocol covering e.g. C11-flumazenil PET with structural MR-imaging (T_1-weighted, T_2-weighted), UTE (ultra-short echo time) sequence for attenuation correction, diffusion tensor imaging, spectroscopy and task-related fMRI, as well as resting state fMRI in a time frame of 60 min total acquisition time is feasible. Moreover, this combination of MR and PET yields results with highly specific molecular information and superb spatial resolution but the temporal aspect, in the sub-second range, is still missing. This is where implementation of EEG recording in the hybrid MR–PET scanner is useful. As described in the preceding section, the EEG signal is modulated by task/patient/pharmacological manipulations on a millisecond timescale allowing investigation of rapid fluctuations in brain dynamics reflecting functional changes. Integration of all three methods allows a more comprehensive understanding of brain function.

The trimodal approach of integrating an MR-compatible EEG-system in the hybrid 3 T MR–PET system has been successfully implemented. The PET electronics do not disturb the electrophysiological signals and the attenuation of the PET signals caused by the EEG electrodes is negligible. A trimodal approach holds great promise especially for the investigation of cognitive, social or emotional paradigms using pharmacological challenges. In such experiments, pharmacological intervention might lead to a change in receptor status thereby precluding a second, subsequent run under similar/identical physiological conditions. Additionally, it cannot be discounted that the putative pharmacological challenge might change the cerebrovascular volume and flow thereby modifying the underlying assumptions, the PET parameters, and the BOLD-based measurement. A truly simultaneous approach ensures the same physiological conditions for all measurements and, additionally, allows investigation of perfusion changes via MR-based methods such as arterial spin labelling (ASL).

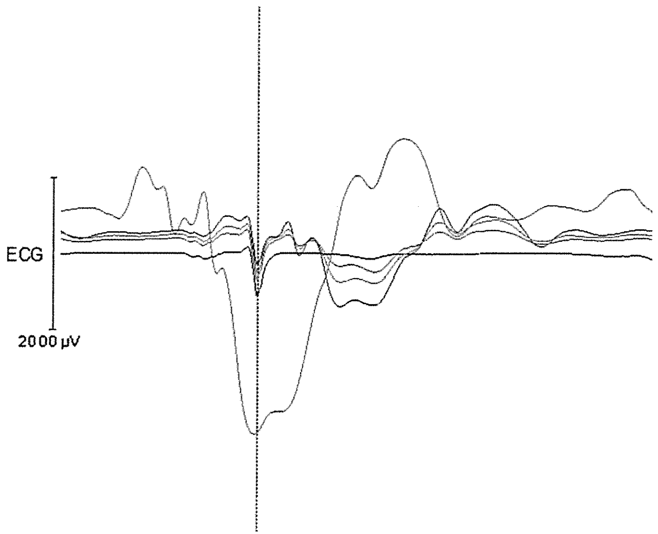

Fig. 7. The ECG signal at different field strengths, illustrating the increase in amplitude and signal distortion as field strength increases. Black corresponds to 0 T, purple to 4 T, green to 7 T, blue to 8 T and red to 9.4 T.

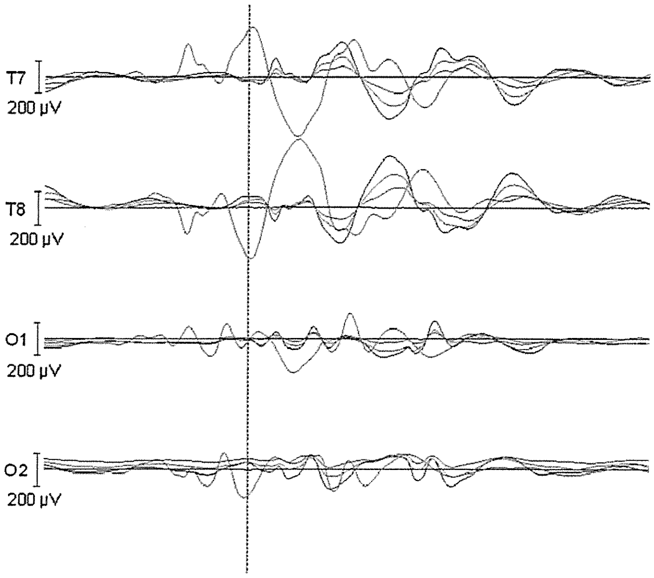

Fig. 8. EEG signal at temporal and occipital electrodes at different field strengths, illustrating the increase in amplitude and signal distortion as field strength increases. Black corresponds to 0 T, purple to 4 T, green to 7 T, blue to 8 T and red to 9.4 T.

2.5. Multimodal Imaging at 9.4 T

Notwithstanding the ubiquity of 3 T MRI or the utility of hybrid MR–PET at 3 T, the tantalising prospect of hybrid MR–PET at 9.4 T holds great promise. In the pursuit of this endeavour, however, a number of hurdles must be overcome and the first of these is 'straightforward' high-resolution, proton-based imaging at this high field strength. Thereafter, combining ultra-high spatial resolution structural imaging with non-proton imaging and spectroscopy simultaneously with PET and EEG could open up new horizons. The prospects and perspectives for the feasibility of multimodal MR–PET–EEG at 9.4 T are explored and the results from initial investigations are presented in the following.

2.6. High-resolution, structural imaging with ultra-high field MRI

A particular strength of ultra-high field MRI is the opportunity to focus on specific brain regions in great detail. The cerebellum may be taken as an example for illustrative purposes. The importance of the cerebellum and its major role in movement control and in cognitive-emotional processing are well known [39] with multiple cerebellar functions integrated in the cortical layer. The cerebellar cortex can be affected by many neurological and psychiatric disorders, such as stroke, tumours, autism, and schizophrenia [39,40].

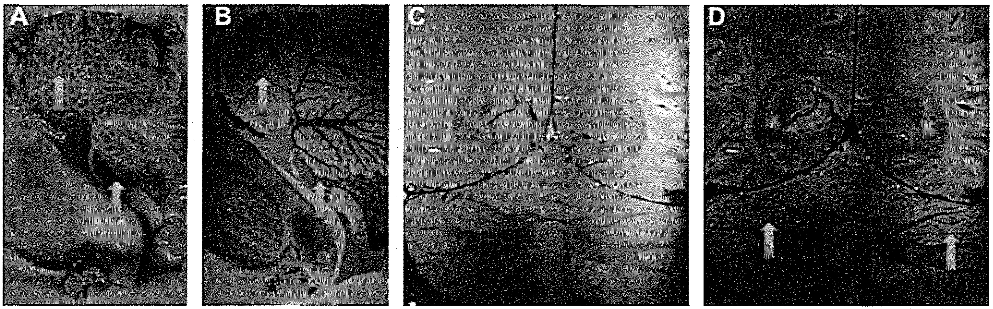

Fig. 9. MRI of cerebellum at 9.4 T. (A and B) Phase and magnitude images of fixed tissue. The granular and molecular layers have distinct phase, T_2^* and M_0 contrast. (C and D) *In vivo* imaging at 9.4 T using a 2D multiple-echo gradient echo sequence. Anisotropic resolution of 0.2 × 0.2 × 1.5 mm^3. TR = 120 ms, TE = 6.5 ms (C), 17.5 ms (D), 70°. At closer inspection, in regions where the slice orientation is favourable, the cerebellar grey matter shows two layers with distinct T_2^* properties.

The convoluted structure of the cortical layer is divided into three layers, from the inside to the outside, as follows: granular, Purkinje, and molecular. Genetic disorders such as ataxias [39] and aceruloplasminemia [41], in which layer dependent variations in iron deposition have been shown using histological examination [42], also affect this region. Therefore, non-invasive methods delivering precise anatomical images of the cerebellar cortical architecture could potentially provide new markers for diagnosis and follow-up. In the results demonstrated below, an adaptation of a 2D protocol [43] for 9.4 T has been extended to establish a 3D protocol where visualisation of layers is possible irrespective of their orientation with respect to the imaging plane. This is shown in Figs. 9 and 10. The visibility of cerebellar layers is striking in (0.2 mm)^3 imaging of fixed tissue. Through quantitative imaging we can attribute the contrast to different M_0, and structural (iron content, cell size and packing) properties of the molecular and granular layers. Both phase and magnitude contrasts are shown in Fig. 9A and B. Despite the use of relatively thick slices (1.5 mm), glimpses of layer structure can be gained in 2D images *in vivo* (Fig. 9C and D), but only for regions where the slice orientation is favourable. This limitation is eliminated in 3D imaging with (0.32 mm)^3 isotropic resolution, shown in Fig. 10. In this example, the echo time is shorter than that required for maximum contrast in order to avoid blurring due to signal misregistration by background field gradients. With improved shimming, acquisition at a longer TE will improve layer visibility and bring imaging of cerebellar layers into 9.4 T MRI routine.

The availability of hardware capable of parallel transmit allows the development and use of advanced imaging techniques at 9.4 T. In general, ultra-high field MRI opens up the opportunity for MR microscopy *in vivo*. However, high spatial encoding mandates long acquisition times. In addition to the use of rapid imaging techniques, one may address this problem by reducing the region-of-interest by means of selective excitation. The pioneering work in the field of spatially-selective excitation of arbitrary regions [44] indicates reduction of the complexity of the Bloch dynamics to yield a solvable linear system with two drawbacks: (i) one has to deal with an inverse problem, and (ii) its applicability to flip angles beyond a few degrees is limited when Nyquist acceleration is considered, which is generally the case. While inverse solutions come with all too well known hurdles such as numerical accuracy and the need for regularisation [45–50], MRI at ultra-high field would be significantly impaired if large flip angle excitations are excluded.

A more recent approach [51] exploits the notion that an appropriately designed MR signal acquisition or simulation of a spin

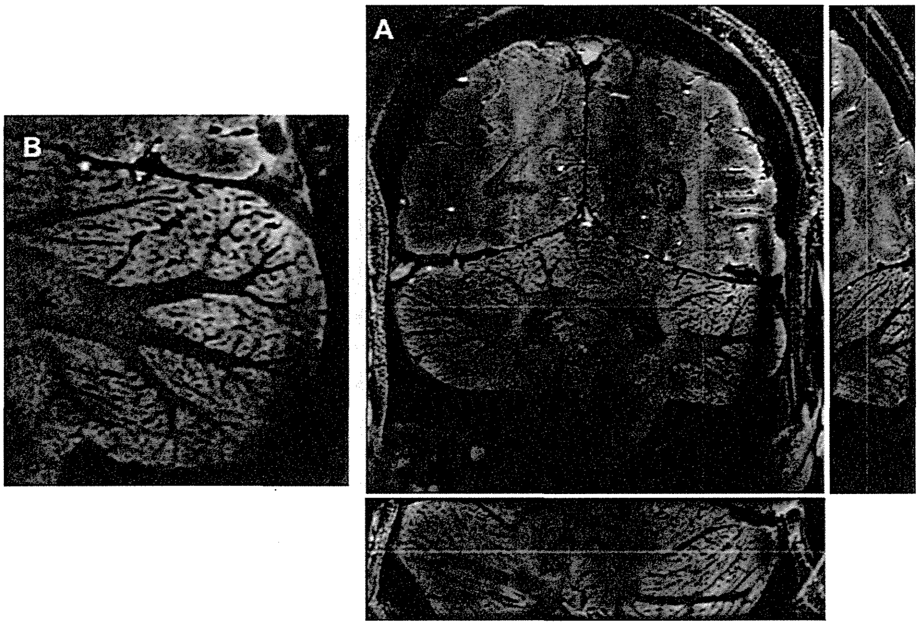

Fig. 10. A detailed view of the cerebellum imaged at 9.4 T. (A and B) *In vivo* imaging at 9.4 T using a 3D GRE sequence. Resolution of 0.32 mm isotropic. TR = 28 ms, TE = 14 ms, 25 deg. Right: orthogonal views of a 3D slab including the occipital cortex and the cerebellum. Left: magnified region.

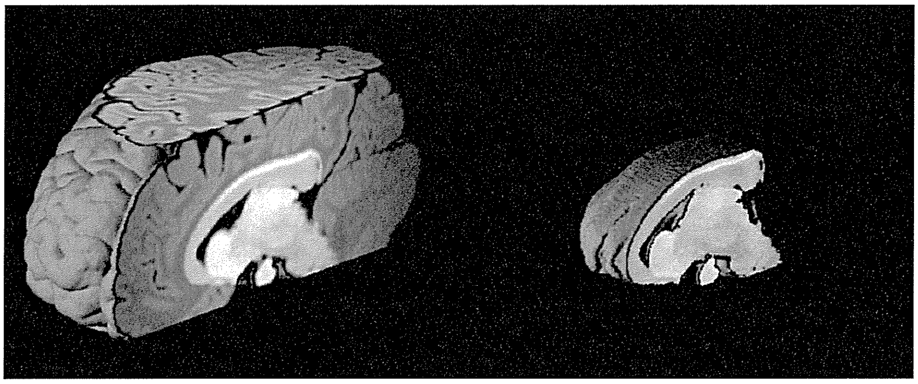

Fig. 11. The figure compares full and zoomed FOV GRE images obtained after global and 3D selective excitation. Both volumes were acquired within the identical measurement time whereby the zoomed image exhibits a spatial resolution that is a factor of two better in all three dimensions.

population which resembles the desired target pattern, is in accordance with the mirrored dynamics. A judicially time-reversed, measured signal – which includes off-resonance and T_2 relaxation – provides an RF pulse that will, in reality, excite the desired target pattern. By reversing problem formulation, as opposed to inverting the mathematical formulation while considering the z-magnetisation, the above problems are addressed. The results obtained with this approach are presented in Fig. 11.

2.7. Metabolic imaging of ^{23}Na, ^{17}O, and ^{31}P

Sodium, oxygen, and phosphorus are involved in major physiological processes of mammalian cells. These physiological processes are amenable to interrogation by various MR techniques probing the isotopes ^{23}Na, ^{17}O, and ^{31}P which can be employed to gain insight into the metabolism of cells *in vivo* [4,5,52–54].

For the physiological function of cells, the homeostasis of the cellular electrolytes is essential. The Na+/K+-ATPase is an ion pump residing in the plasma membrane which during each cycle actively transports three sodium ions out of the cell and two potassium ions into the cell. It is driven by adenosine triphosphate (ATP) which is hydrolysed into adenosine diphoshate (ADP) and phosphate. Diseases leading to an under-supply of energy to the cell result in a lack of ATP and thus an impairment of the Na+/K+-pump and concomitant water inflow. Hence, cell function and its impairment are reflected in the ratio of intra/extra-cellular sodium and unbound/bound phosphate.

The energy carrier for cell metabolism, ATP, is synthesised via oxidative phosphorylation, in which phosphate bonds to adenosine diphosphate. H_2 from different origins of cell metabolism finally accumulates as water.

In order to make the above-mentioned isotopes readily detectable with MRI, several obstacles have to be overcome. For example, although one can readily image natural abundance $H_2{}^{17}O$ with ultra-high field MRI, one needs to systematically introduce highly enriched ^{17}O gas to modulate the $H_2{}^{17}O$ signal due to the low natural abundance of ^{17}O of only 0.037%.

2.8. Sodium MRI

The second most abundant MR active nucleus in the human body is sodium (^{23}Na). Although its role in the physiology of the human body is fundamental, its low concentration and fast bi-exponential relaxation have always limited its use in neuroimaging. In order to acquire data from the fast decaying component, pulse sequences with short echo times are needed. A comparison has been performed between the gradient echo, 3Dradial-, density adapted 3Dradial, Cones, SPRITE, and twisted projection imaging (TPI) pulse sequence wherein the latter sequence has shown itself to be the most signal-to-noise efficient [55]. In combination with dedicated RF coils, such as phased-array receivers, ultra-high field sodium MRI opens new horizons for the understanding of neurological diseases.

Fig. 12 shows transverse, co-registered slices measured with the same TPI sequence on 9.4 T and 4 T whole-body machines. The sodium image at 4 T (right) shows recognisable CSF but the SNR in tissue is too low to visualise any structures. In contrast, the SNR of the 9.4 T image (left) is very good indeed and is similar to a nominal PET resolution [56].

Single quantum excitation pulse sequences (those described above) yield a strong signal from the CSF, but for medical diagnosis the intracellular sodium is of particular interest. Triple-quantum filtering has been suggested as a means to observe primarily the intracellular sodium [57]. Recently, a single sequence for the integrated acquisition of triple-quantum filtered (TQF) and single quantum (SQ) sodium has been developed [58]. TQF sodium imaging of focal brain ischemia was recently demonstrated on a non-human primate model [59]. In this case, the TQ sodium signal increased in the ischemic hemisphere compared to the contralateral hemisphere shortly after (0.6 h) the onset of ischemia. In contrast, the single quantum signal acquired in the same regions showed only a negligible change. The possibility to measure SQ and TQ signals at the same time will therefore make investigation

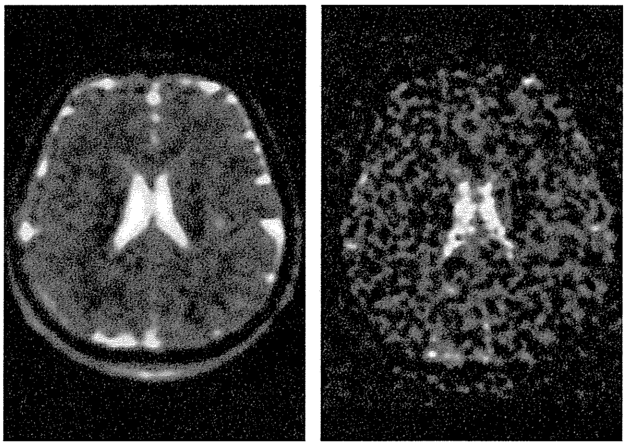

Fig. 12. Sodium distribution in the brain shown in transverse, co-registered slices measured with the same TPI sequence on 9.4 T and 4 T whole-body machines. The sodium image at 4 T (right) shows recognisable CSF but the SNR in tissue is too low to visualise any structures. In contrast, the SNR of the 9.4 T image (left) is very good indeed and is actually better than a nominal PET resolution.

of intracellular sodium a new and real possibility in medical imaging.

3. Discussion

One very significant problem faced in multimodal imaging is the bringing together of the different acquisition timeframes. In fMRI, because of its short acquisition time, EPI is the technique that is most often chosen. In a typical fMRI setup employing a block design, brain function is extracted from a few alternations of the so-called "on–off" cycles. PET, on the other hand, usually requires a longer acquisition time and there is no cycling in the form of a block design. It is clear then, that a simple-minded approach to hybrid MR–PET in this way will not achieve usable results. However, it may be argued that attempting to measure brain function with two complementary modalities is to miss the point. It is important to extract different information from the two modalities such as tumour extent from PET and perfusion or functional localisation from MRI.

For organs such as the brain, which can be regarded as a rigid object for the purposes of image registration, the value of hybrid, simultaneous MR–PET can indeed be questioned. After all, co-registration of datasets acquired on two entirely separate machines is reasonably straightforward. First and foremost, however, when scans are performed in simultaneous mode, patient/subject compliance increases significantly since the patient has to undergo only one examination; dropout rates for a second examination, which can be high depending on how sick the patient is, are no longer a consideration since both scans run simultaneously. In scientific terms, however, the strength of hybrid scanning comes from the fact that the *same physiological conditions* pertain for both datasets. For example, it is known in receptor density mapping using PET that the lack of information about perfusion is a very significant confound. In hybrid mode, this problem can be elegantly addressed by using PET to measure receptor density (where MRI is simply unable to compete) and MRI to measure perfusion as well as running other sequences. Further, under the same physiological conditions, it becomes possible to examine glucose utilisation with FDG and simultaneously carry out a measurement with MRI using, say, ^{31}P as the nucleus of interest, to obtain information on ATP/ADP turnover rates. A comprehensive metabolic workup can thus be achieved if ^{17}O and ^{23}Na are also used although clearly the demands on the hardware will increase substantially.

In order for PET to be quantitative, a major prerequisite is accurate attenuation correction. In contrast to classical PET, where attenuation correction is based on a transmission scan measured with a source typically filled with ^{68}Ge, or in PET/CT where the attenuation map is measured by CT, hybrid MR–PET does not offer the possibility of transmission scanning. The use of T_1-weighted MR images obtained with MPRAGE or FLASH has been investigated to produce attenuation maps. However, unlike CT there is no obvious relationship between the MR image intensity and the attenuation coefficient valid for 511 keV photons. Several solutions for MR-based attenuation are reported in the literature.

Template-based methods utilising attenuation maps obtained from classical PET-based transmission scans have already been proposed for situations where a transmission scan is not available [60]. Such a template-based approach which includes bone per se and which can easily been included in the workflow of the reconstruction of PET images from a hybrid MR–PET scanner has been developed in Juelich [61]. A 3D template derived from the averaged MPRAGE datasets from eight different subjects, and a corresponding template of an attenuation map obtained from transmission scans of the same subjects recorded with an HR + PET scanner, is used. Employing Statistical Parametric Mapping (SPM) [62], the MPRAGE template is warped onto the MPRAGE dataset of the patient under investigation. The deformation data derived from SPM are applied to the transmission template derived from the HR + scanner such that an individualised attenuation map is obtained after addition of the attenuation map of the MR coils. The attenuation map of the MR coils is measured by transmission scanning in the HR + PET scanner in a prior, one-off experiment.

An alternative solution suggested by Hofmann et al. [63] employs a database of MR–CT image pairs and the T_1-weighted MR image of the subject to be studied, a pseudo-CT may be determined which fits to the individual brain and is transformed to the desired attenuation map valid for 511 keV photons.

The above-mentioned methods may fail in the presence of bone lesions and deformations since standard MR sequences deliver no signals from bone and air making it impossible to assign the corresponding attenuation data to these compartments. Motivated by the desire to obtain reliable delineation of bone, the use of ultra-short-echo time (UTE) sequences has been proposed [64,65]. UTE images acquired with two echo times of 0.07 and 2.46 ms, for example, differ primarily with regard to bone signal allowing its specific consideration when constructing an attenuation map. Soft tissue and air can be further classified from these images. Comparisons between the UTE-based and CT-based attenuation correction yielded differences for the whole brain of $\sim$5%, but with local differences of up to ±40% [65]. Recently, a four-class tissue segmentation technique combining the UTE approach with the Dixon water-fat technique has been reported [66].

The availability of hybrid MR–PET systems has led to the development of rigid body motion correction techniques for simultaneous MR–PET data acquisition [67,68]. Motion information obtained from MRI data is utilised in the PET image reconstruction process. It is often desirable for such reconstruction methods to group data into "frames" in which motion is negligible; the data in each frame are then effectively free of motion. Segmentation of the continuously recorded list mode stream of PET data then corresponds to the dynamics of head motion and the computational burden required for the motion correction is reduced. Motion tracking of the head in the confines of a hybrid MR–PET scanner presents some challenges which, although not trivial to overcome, can be successfully addressed; tracking using camera-based systems can be employed [69,70].

In the foreseeable future, the domain of ultra-high field MR–PET is likely to be mainly brain imaging; simultaneous MR–PET imaging capability opens up new directions of research, some of which have already been alluded to above, but particularly pharmacological challenge. Brain activation processes, where repetition of the task in a separate scanner will not necessarily employ the same areas or employ them to the same level, will almost certainly be involved. Columnar-level functional resolution from MRI/fMRI combined with tracer information from PET is a very exciting prospect.

This enthusiasm for new avenues of research must, however, be tempered with reality. There are numerous challenges to be faced at ultra-high field. Amongst them, power deposition from the radiofrequency pulses must be very carefully monitored. The use of transmit arrays will undoubtedly help mitigate the problem of inhomogeneous excitation, but these arrays will probably entail more scatter and will attenuate the photons from the point-of-view of PET. Construction and operation of MR-compatible devices to measure blood radioactivity continuously will be concomitantly more challenging. The radiation exposure in PET means that it may be difficult to obtain the necessary approvals for experiments on normal, healthy volunteers. Finally, aside from the regulatory issues relating to ultra-high fields, the issue of patient comfort in a long magnet will inevitably make it more difficult to find compliant volunteers and, in the long run, patients.

4. Perspectives

In order to discuss the research and clinical perspectives of MR–PET, the discussion can be broken down into two parts: (a) 3 T MR–PET and (b) ultra-high field MR–PET.

MR–PET at 3 T is a new clinical technology that is finding its place at a rapid pace; on the order of 100 hybrid, whole-body MR–PET machines have either already been sold or are on order. These machines do not have the same PET spatial resolution of the BrainPET introduced here but they do have a larger bore and are thus capable of hybrid MR–PET of the body. As such, it can be expected that a large number of studies will look into the efficacy of these instruments and technology will be developed to enable co-registration of organs that are not amenable to rigid transformations. The problems associated with attenuation correction remain. Indeed, the methodologies developed for the brain are not easy to carry over and MR-based tissue segmentation remains problematic.

MR–PET measurements related to brain function are the first to benefit from this hybrid modality. Patient/volunteer compliance is an aspect that is not to be underestimated, especially in the clinic where it may simply not be possible to subject the patient to two scans in two different modalities where each one has a probable duration of about an hour.

For research applications, perhaps the obvious way forward, that of measuring the brain function with two different modalities, is not recommended. Rather, the aim of paradigm developers has to be to exploit the strengths of each modality and to engage, for example, in experiments where "novelty" would be lost through training effects if two separate scans had to be performed in two different scanners. Importantly, in such a construct, the *same physiological conditions* pertain to both sets of data acquired in a hybrid scanner. Another area of application is pharmacological MRI; here, the pharmaceutical agent could be labelled and its distribution followed with PET during which time MRI could be performed to include, for example, fMRI, DTI, and ASL to obtain information about brain function, anatomical connectivity and perfusion changes, respectively. Furthermore, the addition of EEG to measure changes in neural activity with a high temporal resolution allows for a more complete examination of the effects of pharmacological challenges on brain function when data from all three modalities are integrated.

Finally, there is huge potential for MRI to 'learn' from PET and vice versa. The promise of hybrid MR–PET, in this regard, is illustrated here with preliminary results from an ongoing study looking at simultaneous arterial spin labelling using MRI and $H_2{}^{15}O$ PET. Several studies have compared ASL-MRI and $H_2{}^{15}O$ PET for the evaluation of ASL reliability and reproducibility [71–73]. However, none of the previous studies had the possibility to perform both methods simultaneously to minimise physiological variations. A simultaneous ASL-MRI and $H_2{}^{15}O$ PET approach can be implemented in hybrid MR–PET for a proper quantitative comparison of both methods. $H_2{}^{15}O$ PET is regarded as the "gold standard" for perfusion measurements but requires the injection of a tracer and is not so straightforward to repeat. In contrast, questions remain regarding the accuracy and reproducibility of ASL; a comparison of the two datasets simultaneously in a hybrid scanner would thus bring enormous benefits by freeing up PET for other investigations and leaving the measurement of perfusion to a tested and calibrated ASL measurement. Results from a first, preliminary qualitative comparison of CBF images obtained with both modalities in hybrid mode reveals a basic similarity. Fig. 13 shows how the PET and ASL fit well within the colour scale ranging from 0 to 120 ml/100 g/min. In the ASL images some spatial distortions can be seen. Further analyses remain to be performed in order to examine the correlative relationship between both approaches.

One of the most important features of PET is its ability to provide quantitative images of biological and/or physiological functions. The drawback of the technique is, however, the need for an arterial input function, which requires continuous or frequent blood sampling from the arterial line. Several reports presented the potential of extracting the input function from PET images [76–78], but a critical issue is the ambiguity of the small recovery of the carotid artery, attributed to the insufficient spatial resolution of PET images relative to the structure of the carotid artery lines. The small recovery could be corrected if the inner diameter or the cross section is determined. High resolution MRI would make an important contribution to this, and this will be one of the significant applications of the hybrid MR–PET systems. It was shown that both the volume measured by the black-blood T_1 imaging using 3 T MRI, and the time-of-flight MRA, provided the recovery coefficient that is consistent with the one obtained from quantitative $C^{15}O$-based blood volume images [79]. It should also be noted that these three methods provided quantitative values for cerebral blood flow and cerebral metabolic rate of oxygen that are in good agreement with those with the continuous arterial blood sampling. There was a significant amount of spillover in the carotid artery time-activity curves from the surrounding tissues; spillover correction has also been important, as noted in previous work [80].

In order to further underline the perspectives of multi-modal imaging, the results from another preliminary, on-going MR–PET preoperative study are briefly reported. The aim is to investigate the highly multiparametric MR imaging space for tumour research. Specifically, the visibility of tumour substructure in this high-dimensional space is being investigated. The experience gained from the 3 T hybrid system could open the way for informed decision-making as to which MR contrasts might have the highest impact in high-field MR–PET tumour imaging.

The studied cohort comprises patients with tumours close to cortical areas responsible for motor activity and language. A multiparametric MRI examination was performed simultaneously with FET-PET on the 3 T Siemens hybrid system described above. The MR protocol included high-resolution ($1 \times 1 \times 1$ mm^3) acquisitions: 3D MP-RAGE (T_1-weighted, pre and post-contrast), 3D SPACE (T_2-weighted) and 2D multi-echo GRE (magnitude and phase). Lower-resolution FLAIR, diffusion, perfusion and fMRI information were also obtained. The total acquisition time was 1 h.

In this preliminary analysis, 6 MR-based contrasts were included: three of them are mixed-contrast (MP-RAGE post contrast, SPACE and late-echo GRE, which are T_1, T_2, T_2^* and proton-density-weighted, respectively) and three quantitative maps consisting of magnetic susceptibility, T_2^* and water content.

SPACE is a relatively new turbo-spin-echo-type sequence with very long echo train, the applicability of which to fast 3D tumour visualisation with T_2 contrast has been recognised [81]. The comparison between pre- and post-contrast MP-RAGE intensities provides qualitative information on blood–brain-barrier disturbance and tumour vascularisation. Evidence regarding the usefulness of gradient-echo data with SWI post-processing for tumour characterisation has recently begun to emerge [82,83]. It was thus found that using SWI in conjunction with contrast agent showed intratumoral susceptibility enhancement effects, that were not visible in other MR images, as well as contrast enhancement that is visible with standard MR imaging [83]. The frequency of intralesional susceptibility enhancement was found to correlate with the grade of tumour malignancy determined by both PET and histopathology as the "gold standard". This novel technique may be a promising tool for the noninvasive differentiation of low-grade and high-grade brain tumours; this remains to be proven in a much larger study encompassing many different types of tumours but the perspectives look promising.

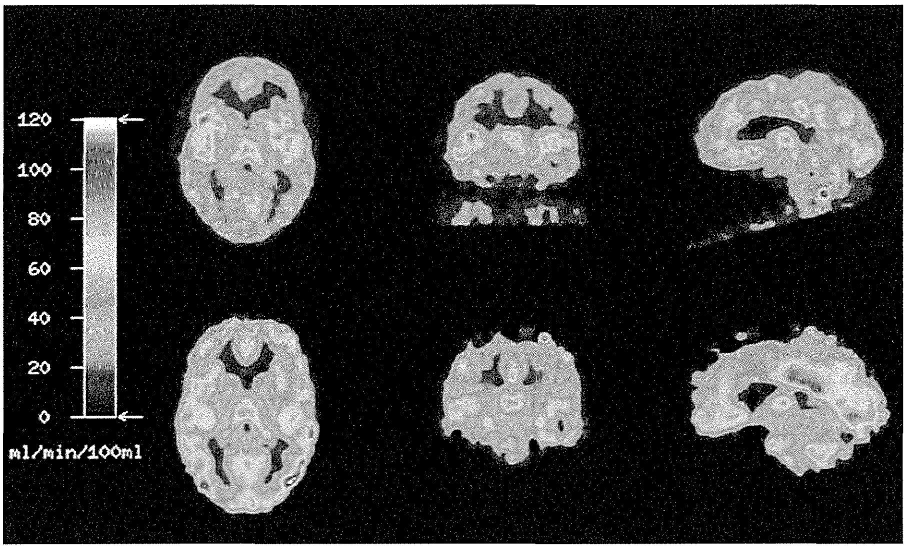

Fig. 13. Comparison of quantified images of cerebral blood flow (CBF) obtained in the hybrid 3 T MR–PET scanner equipped with a BrainPET insert as described above. Top: CBF images (from left to right: transaxial, coronal, sagittal) obtained with PET recorded for 60 s after injection $H_2{}^{15}O$. Bottom: simultaneously obtained CBF images using MRI and ASL. Quantitative measurements of cerebral blood flow with PET and $H_2{}^{15}O$ in comparison to MRI and ASL was performed in the hybrid 3 T BrainPET MR scanner described above. For MRI two dedicated head coils located inside the PET detector were employed, one outer bird cage coil for combined transmit and receive and one inner 8 channel coil for receive, which are both optimized in regard to minimal attenuation for PET, were used. For ASL, a pseudoContinuous Arterial Spin Labelling (pCASL) sequence was used for its higher SNR. pCASL applies a 1.4 s train of RF and gradient pulses to invert the magnetisation of blood water flowing through the labelling plane [74]. In our experiments the position of the labelling plane was selected based on a quickly acquired time-of-flight angiogram to ensure optimal orientation of the carotid and vertebral arteries. A delay of 1 s was inserted between labelling and readout to guarantee blood perfusion of the majority of the voxels. The pre-saturation pulses are applied to the imaging region before labelling to avoid spin perturbation in imaging planes caused by the labelling train. By using readouts with single-shot 2DEPI; 100 measurements with 50 pairs of label-control volumes were obtained. The total measurement time for pCASL acquisitions was 6 min. After 2 min run of pCASL 555 MBq $H_2{}^{15}O$ was injected as PET perfusion tracer and the PET data were recorded for 3 min in listmode. ASL quantification was performed by using ASLtbx in MATLAB [75]. The first 60 s of PET data after the tracer entry into the brain were reconstructed in a summed image so that the autographic method for the calculation of quantitative CBF images could be used. For this purpose an arterial input function was obtained by continuous blood sampling from the radial artery using an MR-compatible blood monitor and corrected for delay and dispersion.

SWI uses a compound magnitude-phase contrast obtained in post-processing and this might mask features which vary in opposite directions in the two contrasts. Here, the full information accessible from a multi-echo GRE is used instead.

Susceptibility, T_2^* and quantitative water content were obtained as follows. Susceptibility mapping was performed starting from phase information. Software developed in-house, following to a large extent the method of de Rochefort [84] was used. From the magnitude information, T_2^* is obtained from a mono-exponential fit of the signal intensity after sinc correction and water content is obtained from the intensity of the signal extrapolated to $TE = 0$ m after transmit and receive efficiency correction and normalisation to CSF [85].

The processing of multiparametric MR information was carried out in a manner similar to that described in [88]. Briefly, after coregistration, each contrast was normalised to the mean of its histogram and the multiparametric space is described using its principal components. This can be performed for the whole volume or separately for specific ROIs. Finally, clustering was performed on the most significant principal components.

The results obtained with the above procedure are illustrated in Fig. 14. Different MR contrasts are shown for a representative slice, complemented by the FET-PET results (integral intensity over the whole measurement time). The principal components were determined for a ROI containing the tumour. This was carried out for the MR data only (middle row) and for the combined MR and PET data (bottom row). Components with amplitudes above 5% of the main one were kept. Cluster analysis using 9 clusters (MR data only) or 14 clusters (MR and PET data) shows similar structure within the solid tumour (high intensity in PET) as well as substructure in the region considered to be oedema [86].

Interestingly, by using only the tumour delineation observable in T_1-Gd and T_2 images and a bio-mathematical model including cell proliferation and infiltration, Swanson et al. were able to describe trends in survival rates as well as response to radiation therapy for glioblastoma patients [87,88]. The 'gradient' between the delineation of the tumour in T_1-Gd and T_2 images can be expressed in a way involving cell proliferation and infiltration. The signification of the 'gradient' is that the T_1-Gd circumference approximates the edge of the 'solid tumour' and that the T_2 circumference represents not only the extent of oedema but also a zone of a low concentration of 'isolated tumour cells'. That tumour cells extend much farther then even the imageable abnormality is evidenced by malignant cells cultured by Silbergeld and Chicoine [89] from as far as 4 cm away. The relation between tumour delineation and outcome prediction is nonlinear and probably not reflected entirely in the principal component analysis of our study. However, by taking into account additional information about the region considered to be oedema, for example its substructure revealed by clustering analysis and inhomogeneities in its water content, a better discrimination between oedema and cell infiltration might become feasible.

Results obtained on the region corresponding to PET hyperintensity, which is attributed to solid tumour and is to be removed at surgery, are reported here. Water content in normal appearing white and grey matter was compared to water content within the tumour region for 10 patients. The tumour ROI was identified by FET-PET hyper-intensity using simple thresholding. Despite the fact that the tumours studied here were located to a large extent in the white matter, the water content within tumour tissue (84.6%) was found to be very close to that of normal appearing grey matter for the same patients (84.0%) and of comparable variability: standard deviation = 0.8% in tumour tissue versus 0.7% for GM. Interestingly, water content in the normal appearing grey matter in the patients was found to be very close to that of GM in the normal population, but the water content of white matter was slightly

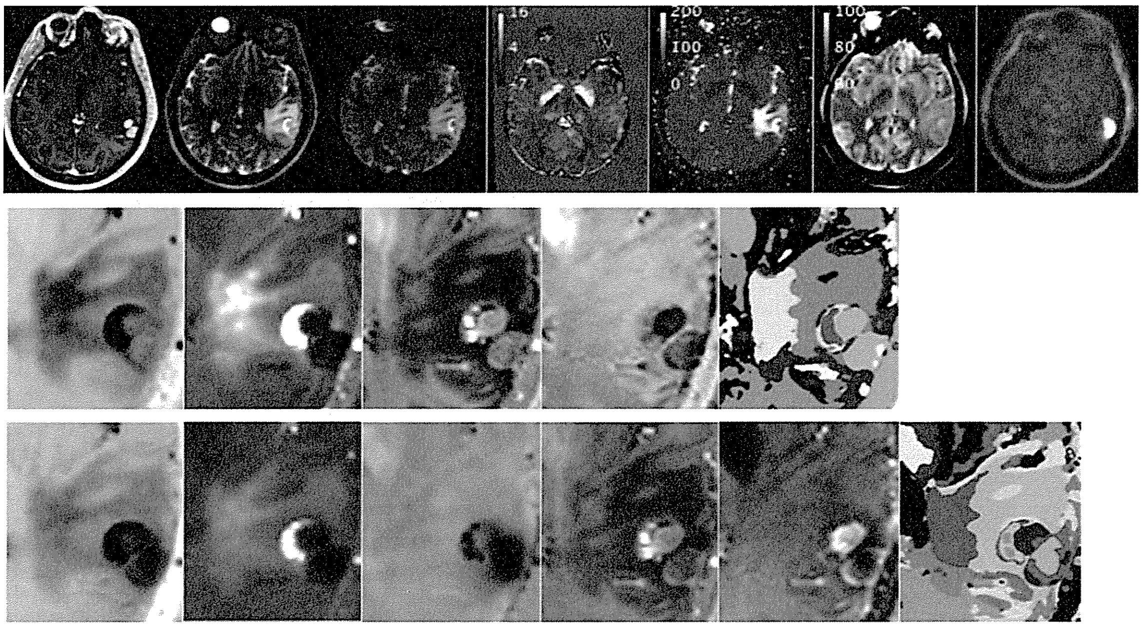

Fig. 14. Upper row: Representative slice with different contrasts or quantities. From left to right: MP-RAGE (post contrast), SPACE, GRE (TE = 50 ms), quantitative susceptibility (a.u.), T_2^* (ms), quantitative water content (%) and FET-PET (a.u.). All MR images have resolution of 1 × 1 × 1 mm^3. Middle row: four most significant principal components (PC) obtained from the MR contrasts for the tumour region. Farthest right: results of *k*-means clustering (9 clusters) on the PC. Bottom row: similar to middle row, when PET data are also included (5 PC, 14 clusters).

higher. Thus, the mean values over the 10 patients were 70.7%(1.1) for WM and 84.0%(0.7) for GM compared to 69.2%(1.7) for WM and 83.7%(1.2) for GM in healthy controls. Given the very tight regulation of water content in healthy tissue, the 1.5% increase in water content found in the normally appearing white matter of patients might be significant. However, since there was a substantial age difference between the volunteers (26 years old on average) and the patients (51 yrs) on which these results were obtained, the issue requires further investigation.

T_2^* contrast was found to be highly efficient in delineating putative substructure within the tumour region. Furthermore, the T_2^* values within the tumour are very different from those of normal tissue and their variability is high. T_2^* contrast at 9.4 T in normal tissue is much richer than at 3 T. The higher equilibrium magnetisation can be used for imaging with small voxel size whilst maintaining a high SNR. The combination of these factors holds promise for the potential increase in usefulness of T_2^* and phase contrast for tumour delineation at 9.4 T.

Irrespective of field strength, the question regarding the significance of the regions found by cluster analysis remains. Further study is required in this respect with the most promising investigation being a comparison between MR-based clusters and regions of different dynamics of the tracer uptake, as reflected by the time-activity curves in PET.

5. Conclusions

The use of hybrid MR–PET technology in humans, at 3 T and at 9.4 T, capable of simultaneous acquisition of MR and PET datasets has been presented and discussed. Clinical and neuroscientific examples from a 3 T MR–PET system underscore the potency of the new scanners. The approach of triple modal imaging by including EEG to cover the temporal dimension has also been elucidated. Use of an ultra-high magnetic field of 9.4 T, together with a PET insert, has also been outlined and feasibility has been shown. Lastly, the potential of new technological advances available at ultra-high field have been discussed. The utility of MR–PET at an ultra-high field of 9.4 T has been demonstrated as has the potential integration of EEG at this field.

The case for multimodal imaging at 3 T and at 9.4 T is a sound one that brings more advantages than disadvantages.

Acknowledgments

This paper is dedicated to Prof. Hans Herzog who has led the PET group in Juelich over the last 28 years and who has been instrumental in pushing forward the MR–PET and multi-modal imaging activities; we thank him for his enormous contributions and wish him the very best for his retirement!

The authors would like to thank Fabian Keil, Dr. Carolin Weiss, Johannes Lindemeyer, Dr. G. Stoffels and Dr. C. Filss for help in performing some of the aspects of the work reported here. We also thank Martina Bunn for valuable assistance with manuscript preparation.

Funding from the Bundesministerium für Bildung and Forschung (Grant No.: 13N9121) and generous support from Siemens for construction of the 9.4 T MR–PET scanner are gratefully acknowledged.

References

[1] D. Pauleit, G. Stoffels, A. Bachofner, F.W. Floeth, M. Sabel, H. Herzog, L. Tellmann, P. Jansen, G. Reifenberger, K. Hamacher, H.H. Coenen, K.J. Langen, Comparison of (18)F-FET and (18)F-FDG PET in brain tumors, Nucl. Med. Biol. 36 (2009) 779–787.

[2] C.A. Olman, N. Harel, D.A. Feinberg, S. He, P. Zhang, K. Ugurbil, E. Yacoub, Layer-specific fMRI reflects different neuronal computations at different depths in human V1, PLoS One 7 (2012) e32536.

[3] E. Yacoub, P.F. Van De Moortele, A. Shmuel, K. Uğurbil, Signal and noise characteristics of Hahn SE and GE BOLD fMRI at 7 T in humans, NeuroImage 24 (2005) 738–750.

[4] A. Lu, I.C. Atkinson, X.J. Zhou, K.R. Thulborn, PCr/ATP ratio mapping of the human head by simultaneously imaging of multiple spectral peaks with interleaved excitations and flexible twisted projection imaging readout trajectories at 9.4 T, Magn. Reson. Med. (2012).

[5] K.R. Thulborn, A. Lu, I.C. Atkinson, F. Damen, J.L. Villano, Quantitative sodium MR imaging and sodium bioscales for the management of brain tumors, Neuroimaging Clin. N. Am. 19 (2009) 615–624.

[6] X.H. Zhu, N. Zhang, Y. Zhang, X. Zhang, K. Ugurbil, W. Chen, In vivo ^{17}O NMR approaches for brain study at high field, NMR Biomed. 18 (2005) 83–103.

[7] H.P. Schlemmer, B.J. Pichler, M. Schmand, Z. Burbar, C. Michel, R. Ladebeck, K. Jattke, D. Townsend, C. Nahmias, P.K. Jacob, W.D. Heiss, C.D. Claussen, Simultaneous MR/PET imaging of the human brain: feasibility study, Radiology 248 (2008) 1028–1035.

[8] H. Herzog, U. Pietrzyk, N.J. Shah, K. Ziemons, The current state, challenges and perspectives of MR–PET, NeuroImage 49 (2010) 2072–2082.

[9] H. Herzog, K.J. Langen, J. Kaffanke, C. Weirich, I. Neuner, G. Stofels, E. Rota Kops, J. Scheins, L. Tellmann, N.J. Shah, MR–PET opens new horizons in neuroimaging, Future Neurol. 5 (2010) 807–815.

[10] H. Herzog, K.J. Langen, C. Weirich, E. Rota Kops, J. Kaffanke, L. Tellmann, J. Scheins, I. Neuner, G. Stoffels, K. Fischer, L. Caldeira, H.H. Coenen, N.J. Shah, High resolution BrainPET combined with simultaneous MRI, Nuklearmedizin 50 (2011) 74–82.

[11] A. Boss, S. Bisdas, A. Kolb, M. Hofmann, U. Ernemann, C.D. Claussen, C. Pfannenberg, B.J. Pichler, M. Reimold, L. Stegger, Hybrid PET/MRI of intracranial masses: initial experiences and comparison to PET/CT, J. Nucl. Med. 51 (2010) 1198–1205.

[12] I. Neuner, J. Kaffanke, H.J. Langen, E. Rota Kops, L. Tellmann, G. Stoffels, C. Weirich, C. Filss, H. Herzog, N.J. Shah, Multimodal imaging utilising integrated MR–PET for human brain tumour assessment, Eur. Radiol., in press. http://dx.doi.org/10.1007/s00330-012-2543-x.

[13] W.D. Heiss, P. Raab, H. Lanfermann, Multimodality assessment of brain tumors and tumor recurrence, J. Nucl. Med. 52 (2011) 1585–1600.

[14] M. Julià-Sapé, I. Coronel, C. Majós, A.P. Candiota, M. Serrallonga, M. Cos, C. Aguilera, J.J. Acebes, J.R. Griffiths, C. Arús, Prospective diagnostic performance evaluation of single-voxel (1) H MRS for typing and grading of brain tumours, NMR Biomed. 25 (2012) 661–673;
W.D. Heiss, P. Raab, H. Lanfermann, Multimodality assessment of brain tumors and tumor recurrence, J. Nucl. Med. 52 (2011) 1585–1600.

[15] C. Majos, M. Julia-Sape, J. Alonso, M. Serrallonga, C. Aguilera, J.J. Acebes, C. Arús, J. Gili, Brain tumor classification by proton MR spectroscopy: comparison of diagnostic accuracy at short and long TE, Am. J. Neuroradiol. 25 (2004) 1696–1704.

[16] G. Widhalm, M. Krssak, G. Minchev, A. Wöhrer, T. Traub-Weidinger, T. Czech, S. Asenbaum, C. Marosi, E. Knosp, J.A. Hainfellner, D. Prayer, S. Wolfsberger, Value of 1H-magnetic resonance spectroscopy chemical shift imaging for detection of anaplastic foci in diffusely infiltrating gliomas with non-significant contrast-enhancement, J. Neurol. Neurosurg. Psychiatry 82 (2011) 512–520.

[17] A.S. Bick, A. Mayer, N. Levin, From research to clinical practice: implementation of functional magnetic imaging and white matter tractography in the clinical environment, J. Neurol. Sci. 312 (2012) 158–165.

[18] A. Boss, A. Kolb, M. Hofmann, S. Bisdas, T. Nägele, U. Ernemann, L. Stegger, C. Rossi, H.P. Schlemmer, C. Pfannenberg, M. Reimold, C.D. Claussen, B.J. Pichler, U. Klose, Diffusion tensor imaging in a human PET/MR hybrid system, Invest. Radiol. 45 (2010) 270–274.

[19] C. Stippich, N. Rapps, J. Dreyhaupt, A. Durst, B. Kress, E. Nennig, V.M. Tronnier, K. Sartor, Localizing and lateralizing language in patients with brain tumors: feasibility of routine preoperative functional MR imaging in 81 consecutive patients, Radiology 243 (2007) 828–836.

[20] P.A. Bandettini, E.C. Wong, R.S. Hinks, R.S. Tikofsky, J.S. Hyde, Time course EPI of human brain function during task activation, Magn. Reson. Med. 25 (1992) 390–397.

[21] S. Ogawa, D.W. Tank, R. Menon, J.M. Ellermann, S.G. Kim, H. Merkle, K. Ugurbil, Intrinsic signal changes accompanying sensory stimulation: functional brain mapping with magnetic resonance imaging, Proc. Natl. Acad. Sci. U. S. A. 89 (1992) 5951–5955.

[22] S. Debener, M. Ullsperger, M. Siegel, A.K. Engel, Single-trial EEG–fMRI reveals the dynamics of cognitive function, Trends Cogn. Sci. 10 (2006) 558–563.

[23] R.J. Huster, S. Debener, T. Eichele, C.S. Herrmann, Methods for simultaneous EEG–fMRI: an introductory review, J. Neurosci. 32 (2012) 6053–6060.

[24] H. Laufs, Endogenous brain oscillations and related networks detected by surface EEG-combined fMRI, Hum. Brain Mapp. 29 (2008) 762–769.

[25] B. Biswal, F.Z. Yetkin, V.M. Haughton, J.S. Hyde, Functional connectivity in the motor cortex of resting human brain using echo-planar MRI, Magn. Reson. Med. 34 (1995) 537–541.

[26] M.E. Raichle, A.M. MacLeod, A.Z. Snyder, W.J. Powers, D.A. Gusnard, G.L. Shulman, A default mode of brain function, Proc. Natl. Acad. Sci. U. S. A. 98 (2001) 676–682.

[27] C.G. Benar, C. Grova, E. Kobayashi, A.P. Bagshaw, Y. Aghakhani, F. Dubeau, J. Gotman, EEG–fMRI of epileptic spikes: concordance with EEG source localization and intracranial EEG, NeuroImage 30 (2006) 1161–1170.

[28] A.P. Bagshaw, T. Warbrick, Single trial variability of EEG and fMRI responses to visual stimuli, NeuroImage 38 (2007) 280–292.

[29] I. Neuner, T. Stocker, T. Kellermann, V. Ermer, H.P. Wegener, S.B. Eickhoff, F. Schneider, N.J. Shah, Electrophysiology meets fMRI: neural correlates of the startle reflex assessed by simultaneous EMG–fMRI data acquisition, Hum. Brain. Mapp. 31 (2010) 1675–1685.

[30] T. Warbrick, A. Mobascher, J. Brinkmeyer, F. Musso, N. Richter, T. Stoecker, G.R. Fink, N.J. Shah, G. Winterer, Single-trial P3 amplitude and latency informed event-related fMRI models yield different BOLD response patterns to a target detection task, NeuroImage 47 (2009) 1532–1544.

[31] J. Fell, Cognitive neurophysiology: beyond averaging, NeuroImage 37 (2007) 1069–1072.

[32] S. Sadaghiani, G. Hesselmann, K.J. Friston, A. Kleinschmidt, The relation of ongoing brain activity, evoked neural responses, and cognition, Front. Syst. Neurosci. 4 (2010) 20.

[33] K. Mullinger, R. Bowtell, Combining EEG and fMRI, Methods Mol. Biol. 711 (2011) 303–326.

[34] P.J. Allen, O. Josephs, R. Turner, A method for removing imaging artifact from continuous EEG recorded during functional MRI, NeuroImage 12 (2000) 230–239.

[35] R.K. Niazy, C.F. Beckmann, G.D. Iannetti, J.M. Brady, S.M. Smith, Removal of FMRI environment artifacts from EEG data using optimal basis sets, NeuroImage 28 (2005) 720–737.

[36] S. Debener, K.J. Mullinger, R.K. Niazy, R.W. Bowtell, Properties of the ballistocariogram artefact as revealed by EEG recordings at 1.5, 3 and 7 T static magnetic field strength, Int. J. Psychophysiol. 67 (2008) 189–199.

[37] T. Eichele, V.D. Calhoun, S. Debener, Mining EEG–fMRI using independent component analysis, Int. J. Psychophysiol. 73 (2009) 53–61.

[38] I. Neuner, T. Warbrick, A. Celik, J. Felder, M. Reske, F. Boers, N.J. Shah, EEG acquisition in ultra high static magnetic fields up to 9.4 T, NeuroImage, 2012, in press, http://dx.doi.org/10.1016/j.neuroimage.2012.11.064.

[39] J.D. Schmahmann, Disorders of the cerebellum: ataxia, dysmetria of thought, and the cerebellar cognitive affective syndrome, J. Neuropsychiatry Clin. Neurosci. 16 (2004) 367–378.

[40] M. Steinlin, Cerebellar disorders in childhood: cognitive problems, Cerebellum 7 (2008) 607–610.

[41] M. Grisoli, A. Piperno, L. Chiapparini, R. Mariani, M. Savoiardo, MR imaging of cerebral cortical involvement in aceruloplasminemia, Am. J. Neuroradiol. 26 (2005) 657–661.

[42] B.N. Patel, R.J. Dunn, S.Y. Jeong, Q. Zhu, J.P. Julien, S. David, Ceruloplasmin regulates iron levels in the CNS and prevents free radical injury, J. Neurosci. 22 (2002) 6578–6586.

[43] J.P. Marques, W. van der Zwaag, C. Granziera, G. Krueger, R. Gruetter, Cerebellar cortical layers: in vivo visualization with structural high-field-strength MR imaging, Radiology 254 (2010) 942–948.

[44] J. Pauly, D. Nishimura, A. Macovski, A k-space analysis of small-tip-angle excitation, J. Magn. Reson. 81 (1989) 43–56.

[45] C.Y. Yip, J.A. Fessler, D.C. Noll, A constrained minimization approach to designing multi-dimensional, spatially selective RF pulses, Proc. Intl. Soc. Mag. Res. Med. (2004) 188.

[46] U. Katscher, P. Börnert, C. Leussler, J.S. van den Brink, Transmit SENSE, Magn. Reson. Med. 49 (2003) 144–150.

[47] Y. Zhu, Parallel excitation with an array of transmit coils, Magn. Res. Med. 51 (2004) 775–784.

[48] W. Grissom, C.Y. Yip, Z. Zhang, V.A. Stenger, J.A. Fessler, D.C. Noll, Spatial domain method for the design of RF pulses in multicoil parallel excitation, Magn. Reson. Med. 56 (2006) 620–629.

[49] W.A. Grissom, J.A. Fessler, D.C. Noll, Time-segmented spin domain method for fast large-tip-angle RF pulse design in parallel excitation, Proc. Intl. Soc. Mag. Res. Med. (2007) 676.

[50] K. Setsompop, L.L. Wald, V. Alagappan, B. Gagoski, F. Hebrank, U. Fontius, F. Schmitt, E. Adalsteinsson, Parallel RF transmission with eight channels at 3 Tesla, Magn. Reson. Med. 56 (2006) 1163–1171.

[51] K. Vahedipour, N.J. Shah, T. Stöcker, Direct method for parallel transmit pulse design by time-reversal of the small-tip angle excitation, Proc. Intl. Soc. Mag. Reson. Med 20 (2012) 637.

[52] F.E. Boada, G. LaVerde, C. Jungreis, E. Nemoto, C. Tanase, I. Hancu, Loss of cell ion homeostasis and cell viability in the brain: what sodium MRI can tell us, Curr. Top. Dev. Biol. 70 (2005) 77–101.

[53] R. Ouwerkerk, K. Bleich, J. Gillen, M. Pomper, Tissue sodium concentration in human brain tumors as measured with ^{23}Na MR imaging, Radiology 227 (2003) 529–537.

[54] M. Horn, C. Weidensteiner, H. Scheffer, M. Meininger, M. de Groot, H. Remkes, et al., Detection of myocardial viability based on measurement of sodium content: a (23)Na-NMR study, Magn. Reson. Med. 45 (2001) 756–764.

[55] S. Romanzetti, C.C. Mirkes, D.P. Fiege, A. Celik, J. Felder, N.J. Shah, A comparison of imaging sequences for sodium MR imaging on a 9.4 T whole body machine, Proc. Intl. Soc. Mag. Reson. Med. 19 (2011) 1493.

[56] S. Romanzetti, D. Fiege, J. Felder, A. Celik, C. Mirkes, N.J. Shah, Ultra-high field sodium imaging of the human brain at 9.4 Tesla, Proc. Intl. Soc. Mag. Reson. Med. 20 (2012) 4419.

[57] P.M. Winter, N. Bansal, Triple-quantum-filtered (23)Na NMR spectroscopy of subcutaneously implanted 9l gliosarcoma in the rat in the presence of TmDOTP(5-1), J. Magn. Reson. 152 (2001) 70–78.

[58] D.P. Fiege, S. Romanzetti, C. Mirkes, D. Brenner, N.J. Shah, Simultaneous single-quantum and triple-quantum-filtered MRI of 23Na (SISTINA), Magn. Reson. Med. (2012).

[59] G. LaVerde, E. Nemoto, C. Jungreis, C. Tanase, F.E. Boada, Serial triple quantum sodium MRI during non-human primate focal brain ischemia, Magn. Reson. Med. 57 (2007) 201–205.

[60] M.L. Montandon, H. Zaidi, Atlas-guided non-uniform attenuation correction in cerebral 3D PET imaging, NeuroImage 25 (2005) 278–286.

[61] E. Rota Kops, H. Herzog, Template based attenuation correction for PET in MR–PET scanners, IEEE NSS Conf. Rec. (2008) 3786–3789.

[62] J. Ashburner, K.J. Friston, Nonlinear spatial normalization using basis functions, Hum. Brain Mapp. 7 (1999) 254–266.

[63] M. Hofmann, F. Steinke, V. Scheel, G. Charpiat, J. Farquhar, P. Aschoff, M. Brady, B. Schölkopf, B.J. Pichle, MRI-based attenuation correction for PET/MRI: a novel

approach combining pattern recognition and atlas registration, J. Nucl. Med. 49 (2008) 1875–1883.

[64] C. Catana, A. van der Kouwe, T. Benner, C.J. Michel, M. Hamm, M. Fenchel, B. Fischl, B. Rosen, M. Schmand, A.G. Sorensen, Toward implementing an MRI-based PET attenuation–correction method for neurologic studies on the MR–PET brain prototype, J. Nucl. Med. 51 (2010) 1431–1438.

[65] V. Keereman, Y. Fierens, T. Broux, Y. De Deene, M. Lonneux, S. Vandenberghe, MRI-based attenuation correction for PET/MRI using ultrashort echo time sequences, J. Nucl. Med. 51 (2010) 812–818.

[66] Y. Berker, J. Franke, A. Salomon, M. Palmowski, H.C. Donker, Y. Temur, F.M. Mottaghy, C. Kuhl, D. Izquierdo-Garcia, Z.A. Fayad, F. Kiessling, V. Schulz, MRI-based attenuation correction for hybrid PET/MRI systems: a 4-class tissue segmentation technique using a combined ultrashort-echo-time/Dixon MRI sequence, J. Nucl. Med. 53 (2012) 796–804.

[67] C. Catana, T. Benner, A. van der Kouwe, L. Byars, M. Hamm, D.B. Chonde, C.J. Michel, G. El Fakhri, M. Schmand, A.G. Sorensen, MRI-assisted PET motion correction for neurologic studies in an integrated MR–PET scanner, J. Nucl. Med. 52 (2011) 154–161.

[68] M. Ullisch, C. Weirich, J. Scheins, E. Rota Kops, A. Celik, T. Stöcker, N.J. Shah, A MR-based PET motion correction procedure for simultaneous MR–PET neuroimaging of human brain, PLoS One, 7 (2012) e48149.

[69] J. Schulz, T. Siegert, E. Reimer, C. Labadie, J. Maclaren, M. Herbst, M. Zaitsev, R. Turner, An embedded optical tracking system for motion-corrected magnetic resonance imaging at 7 T, MAGMA, in press. http://dx.doi.org/10.1007/s10334-012-0320-0.

[70] J. Maclaren, M. Herbst, O. Speck, M. Zaitsev, Prospective motion correction in brain imaging: a review, Magn. Reson. Med., in press. http://dx.doi.org/10.1002/mrm.24314.

[71] R.P.H. Bokkers, J.P. Bremmer, B.N.M. van Berckel, A.A. Lammertsma, J. Hendrikse, J.P. Pluim, L.J. Kappelle, R. Boellaard, C.J.M. Klijn, Arterial spin labeling perfusion mri at multiple delay times: a correlative study with H(2)(15)O positron emission tomography in patients with symptomatic carotid artery occlusion, J. Cereb. Blood Flow Metab. 30 (2010) 222–229.

[72] G. Xu, H.A. Rowley, G. Wu, D.C. Alsop, A. Shankaranarayanan, M. Dowling, B.T. Christian, T.R. Oakes, S. Johnson, Reliability and precision of pseudo-continuous arterial spin labeling perfusion MRI on 3.0 T and comparison with ^{15}O-water PET in elderly subjects at risk for Alzheimer's disease, NMR Biomed. 23 (2010) 286–293.

[73] O.M. Henriksen, H.B.W. Larsson, A.E. Hansen, J.M. Grüner, I. Law, E. Rostrup, Estimation of intersubject variability of cerebral blood flow measurements using MRI and positron emission tomography, J. Magn. Reson. Imaging 35 (2012) 1290–1299.

[74] T. Okell, M.A. Chappell, M.W. Woolrich, M. Günther, D.A. Feinberg, P. Jezzard, Vessel-encoded dynamic magnetic resonance angiography using arterial spin labelling, Magn. Reson. Med. 64 (2010) 698–706.

[75] Z. Wang, G.K. Aguirre, H. Rao, J. Wang, M.A. Fernández-Seara, A.R. Childress, J.A. Detre, Empirical optimization of ASL data analysis using an ASL data processing toolbox: ASLtbx, Magn. Reson. Imaging 26 (2008) 261–269.

[76] K. Chen, D. Bandy, E. Reiman, S.C. Huang, M. Lawson, D. Feng, L.S. Yun, A. Palant, Noninvasive quantification of the cerebral metabolic rate for glucose using positron emission tomography, ^{18}F-fluoro-2-deoxyglucose, the Patlak method, and an image-derived input function, J. Cereb. Blood Flow Metab. 18 (1998) 716–723.

[77] S.M. Sanabria-Bohorquez, A. Maes, P. Dupont, G. Bormans, T. de Groot, A. Coimbra, W. Eng, T. Laethem, I. De Lepeleire, J. Gambale, J.M. Vega, H.D. Burns, Image-derived input function for [11C]flumazenil kinetic analysis in human brain, Mol. Imaging Biol. 5 (2003) 72–78.

[78] B.J. Lopresti, W.E. Klunk, C.A. Mathis, J.A. Hoge, S.K. Ziolko, X. Lu, C.C. Meltzer, K. Schimmel, N.D. Tsopelas, S.T. DeKosky, J.C. Price, Simplified quantification of Pittsburgh compound B amyloid imaging PET studies: a comparative analysis, J. Nucl. Med. 46 (2005) 1959–1972.

[79] S. Iguchi, Y. Hori, T. Moriguchi, N. Morita, A. Yamamoto, K. Koshino, H. Kawashima, T. Zeniya, J. Enmi, H. Iida, Verification of a semi-automated MRI-guided technique for non-invasive determination of the arterial input function in ^{15}O-labeled gaseous PET, Nucl. Instrum. Methods Phys. Res., Sect. A, in press.

[80] J.E. Mourik, M. Lubberink, A. Schuitemaker, N. Tolboom, B.N.M. van Berckel, A.A. Lammertsma, R. Boellaard, Image-derived input functions for PET brain studies, Eur. J. Nucl. Med. Mol. Imaging 36 (2009) 463–471.

[81] Y. Kato, S. Higano, H. Tamura, S. Mugikura, A. Umetsu, T. Murata, S. Takahashi, Usefulness of contrast-enhanced T1-weighted sampling perfection with application-optimized contrasts by using different flip angle evolutions in detection of small brain metastasis at 3 T MR imaging: comparison with magnetization-prepared rapid acquisition of gradient echo imaging, Am. J. Neuroradiol. 30 (2009) 923–929.

[82] K. Pinker, I.M. Noebauer-Huhmann, I. Stavrou, R. Hoeftberger, P. Szomolanyi, G. Karanikas, M. Weber, A. Stadlbauer, E. Knosp, K. Friedrich, S. Trattnig, High-resolution contrast-enhanced, susceptibility-weighted MR imaging at 3 T in patients with brain tumors: correlation with positron-emission tomography and histopathologic findings, Am. J. Neuroradiol. 28 (2007) 1280–1286.

[83] V. Sehgal, Z. Delproposto, E.M. Haacke, K.A. Tong, N. Wycliffe, D.K. Kido, Y. Xu, J. Neelavalli, D. Haddar, J.R. Reichenbach, Clinical applications of neuroimaging with susceptibility-weighted imaging, J. Magn. Reson. Imaging 22 (2005) 439–450.

[84] L. de Rochefort, T. Liu, B. Kressler, J. Liu, P. Spincemaille, V. Lebon, J. Wu, Y. Wang, Quantitative susceptibility map reconstruction from MR phase data using bayesian regularization: validation and application to brain imaging, Magn. Reson. Med. 63 (2010) 194–206.

[85] A.M. Oros-Peusquens, F. Keil, Z. Abbas, V. Gras, K.H. Möllenhoff, N.J. Shah, A seven-minute protocol for quantitative, whole-brain, accurate water mapping at 3 T for neuroscientific applications, NeuroImage, submitted for publication.

[86] Y. Yovel, Y. Assaf, Virtual definition of neuronal tissue by cluster analysis of multi-parametric imaging (virtual-dot-com imaging), NeuroImage 35 (2007) 58–69.

[87] K. Swanson, R. Rostomily, E. Alvord, A mathematical modelling tool for predicting survival of individual patients following resection of glioblastoma: a proof of principle, Br. J. Cancer 98 (2008) 113–119.

[88] K.R. Swanson, H.L. Harpold, D.L. Peacock, R. Rockne, C. Pennington, L. Kilbride, R. Grant, J.M. Wardlaw, E.C. Alvord Jr., Velocity of radial expansion of contrast-enhancing gliomas and the effectiveness of radiotherapy in individual patients: a proof of principle, Clin. Oncol. 20 (2008) 301–308.

[89] D.L. Silbergeld, M.R. Chicoine, Isolation and characterization of human malignant glioma cells from histologically normal brain, J. Neurosurg. 86 (1997) 525–531.

Journal of Cerebral Blood Flow & Metabolism (2013) 33, 440–448

www.jcbfm.com

JCBFM Open

ORIGINAL ARTICLE

Rapid quantitative *CBF* and *CMRO*$_2$ measurements from a single *PET* scan with sequential administration of dual ^{15}O-labeled tracers

Nobuyuki Kudomi[1,2], Yoshiyuki Hirano[1], Kazuhiro Koshino[1], Takuya Hayashi[1,6], Hiroshi Watabe[1,7], Kazuhito Fukushima[3], Hiroshi Moriwaki[4], Noboru Teramoto[1], Koji Iihara[5] and Hidehiro Iida[1]

Positron emission tomography (*PET*) with ^{15}O tracers provides essential information in patients with cerebral vascular disorders, such as cerebral blood flow (*CBF*), oxygen extraction fraction (*OEF*), and metabolic rate of oxygen (*CMRO*$_2$). However, most of techniques require an additional C^{15}O scan for compensating cerebral blood volume (*CBV*). We aimed to establish a technique to calculate all functional images only from a single dynamic *PET* scan, without losing accuracy or statistical certainties. The technique was an extension of previous dual-tracer autoradiography (DARG) approach, but based on the basis function method (DBFM), thus estimating all functional parametric images from a single session of dynamic scan acquired during the sequential administration of H$_2^{15}$O and ^{15}O$_2$. Validity was tested on six monkeys by comparing global *OEF* by *PET* with those by arteriovenous blood sampling, and tested feasibility on young healthy subjects. The mean DBFM-derived global *OEF* was 0.57 ± 0.06 in monkeys, in an agreement with that by the arteriovenous method (0.54 ± 0.06). Image quality was similar and no significant differences were seen from DARG; 3.57% ± 6.44% and 3.84% ± 3.42% for *CBF*, and − 2.79% ± 11.2% and − 6.68% ± 10.5% for *CMRO*$_2$. A simulation study demonstrated similar error propagation between DBFM and DARG. The DBFM method enables accurate assessment of *CBF* and *CMRO*$_2$ without additional *CBV* scan within significantly shortened examination period, in clinical settings.

Journal of Cerebral Blood Flow & Metabolism (2013) **33,** 440–448; doi:10.1038/jcbfm.2012.188; published online 12 December 2012

Keywords: acute stroke; brain imaging; cerebral blood flow; kinetic modeling; positron emission tomography

INTRODUCTION

Quantitative cerebral blood flow (*CBF*), oxygen extraction fraction (*OEF*), and metabolic rate of oxygen (*CMRO*$_2$) images can be assessed using positron emission tomography (*PET*) and ^{15}O-labeled radiotracers. These parametric images are essential for understanding the pathophysiological status of cerebral vascular disorders, and this technique has been promoted as a clinical diagnostic tool in some countries. Parametric images have been measured via *PET* by administering multiple ^{15}O-labeled tracers,[1,2] such as in the steady-state method[3,4] or the three-step autoradiography method.[2,5,6] The validity of the technique has been demonstrated with three-step autoradiography on healthy volunteers at rest.[7] An order of 1-hour period, however, is typically required to complete the whole study, because three independent scans are required in addition to > 10-minute intervals between scans to allow for decay of the residual radioactivity of the preceding tracer. Thus, applicability is limited in clinical settings, particularly for patients with acute stroke.[8]

We recently developed a novel *PET* method of dual-tracer autoradiography (DARG)[9] for quantitative assessment of *CBF*, *CMRO*$_2$, *OEF*, and cerebral blood volume (*CBV*), based on sequential administration of dual tracers during a single *PET* scan, with additional *CBV* data obtained from a C^{15}O scan to compensate for radioactivity from the vascular space. The method allows for shortened examination time compared with previous three-step approaches,[9] and was shown to provide quantitative *OEF* values that were in good agreement with those assessed by the arteriovenous oxygen difference in normal monkeys over a wide physiological range, suggesting the validity of quantitative functional values obtained by this method. Of the importance is that the noise property in the calculated functional images by this method is same as that by the three-step autoradiography. A limitation of this method is however attributed to the need for additional C^{15}O scan. An assumption of the fixed fractionations of arterial and venous vasculature components, as has been done in most of other methods could also cause systematic errors in pathological conditions such as the ischemia, which most likely

---

[1]Department of Investigative Radiology, National Cerebral and Cardiovascular Center, Research Institute, Osaka, Japan; [2]Department of Medical Physics, Faculty of Medicine, Kagawa University, Kagawa, Japan; [3]Department of Radiology, National Cerebral and Cardiovascular Center, Osaka, Japan; [4]Department of Neurology, National Cerebral and Cardiovascular Center, Osaka, Japan and [5]Department of Neurosurgery, National Cerebral and Cardiovascular Center, Osaka, Japan. Correspondence: Dr H Iida, Department of Investigative Radiology, National Cerebral and Cardiovascular Center, Research Institute, 5-7-1, Fujishiro-dai, Suita, Osaka 565-8565, Japan.
E-mail: iida@ri.ncvc.go.jp

This study was supported by a Grant from the Ministry of Health, Labor and Welfare (MHLW) of Japan, and also by the Program for Promotion of Fundamental Studies in Health Sciences of the Organization for Pharmaceutical Safety and Research of Japan. NK was supported by the Nakatani Electronic Measuring Technology Association of Japan, by the Ministry of Education, Science, Sports and Culture, Grant-in-Aid for Young Scientists (start-up), 21890171, 2009–2010, and by JSPS KAKENHI (C) Grant number 23590675.

[6]Present address: Kobe MI R&D Center, 6-7-3 Minatojima-minamimachi, Chuo-ku, Kobe, Hyogo 650-0047, Japan.
[7]Present address: Department of Molecular Imaging in Medicine, Osaka University Graduate School of Medicine, 2-2 Yamadaoka, Suita, Osaka 565-0871, Japan.

Received 7 May 2012; revised 19 November 2012; accepted 19 November 2012; published online 12 December 2012

cause dilatation of vasculature and/or the arteriovenous malformation.

In the present study, we developed a formula that eliminates the need for the *CBV* information, which has been required in the previous DARG approach. This computational refinement for the dual-tracer approach has been done using the basis function method (DBFM). Attention was made so as to minimize the systematic errors attributed to the assumption of fixing the arterial- and venous-fractionations. The technique would also be advantageous for significantly shortening the duration of the total clinical examination. The validity of the present method, in terms of quantitative accuracy and quality of generated images, was tested using the data obtained from anesthetized monkeys and young normal volunteers.

THEORY

The present formula was developed to compute *CBF*, $CMRO_2$, and *CBV* simultaneously, thus eliminating the need for additional scan for *CBV* assessment. The distributions of tracer in the vascular space (V_A^W (mL/g) for water and V_0^O (mL/g) for oxygen components) were estimated from dynamic image data acquired during sequential administration of $H_2^{15}O$ and $^{15}O_2$. The kinetics for both $^{15}O_2$ and $H_2^{15}O$ are expressed using the single-tissue compartment model[2] as:

$$Ci(t) = E \cdot f \cdot A_o(t) \otimes e^{\frac{f}{p} \cdot t} + f \cdot A_w(t) \otimes e^{\frac{f}{p} \cdot t} + V_0^o \cdot A_o(t) + V_A^w \cdot A_w(t) \tag{1}$$

where *Ci(t)* (Bq/mL) is the radioactivity concentration in a voxel in a given tissue region, $A_o(t)$ (Bq/mL) and $A_w(t)$ (Bq/mL) are the arterial input functions of ^{15}O-oxygen ($^{15}O_2$) and ^{15}O-water ($H_2^{15}O$) contents, respectively, *f* (mL per minute per gram) is the *CBF*, *E* is the *OEF*, *p* (mL/g) is the blood/brain partition coefficient for water, and ⊗ indicates the convolution integral. The first and second terms on the right side represent the tissue radioactivity of oxygen and water, respectively. The last two terms signify the radioactivity of $^{15}O_2$ and $H_2^{15}O$ in blood vessels. In this study, *p* was fixed at 0.8 mL/g.[10]

The first two terms on the right side in equation (1) have nonlinear relationship with *f*, and we formulated two basis functions[11] to calculate parametric images from the dynamic data. The corresponding basis functions were as follows:

$$\begin{aligned} F_1(f,t) &= f \cdot A_w \otimes e^{-\frac{f}{p} \cdot t} \\ F_2(f,t) &= f \cdot A_o \otimes e^{-\frac{f}{p} \cdot t}. \end{aligned} \tag{2}$$

Equation (1) can then be transformed for each basis function into a linear equation in *E*, V_0^O, and V_A^W as:

$$Ci(t) = F_1 + E \cdot F_2 + V_0^o \cdot A_o + V_A^w \cdot A_w. \tag{3}$$

For the physiologically reasonable range of *f*, that is, $0 < f < 2.0$ mL per minute per gram, 200 discrete values for *f* were given. For a given value of *f*, three values of *E*, V_0^O, and V_A^W were obtained using the standard linear least squares optimization technique. The oprimized *f* value was determined from the 200 discrete values, so that the residual sum of squares between left- and right-hand terms in equation (3) became minimum, thus a unique set of optimized parameters for *f, E*, V_0^O, and V_A^W could be obtained. Metabolic rate of oxygen is then calculated from the obtained *f, E*, and the arterial oxygen concentration. The present formula can be applied to either of the two procedures: $H_2^{15}O$ injection (or $C^{15}O_2$ inhalation) followed by $^{15}O_2$ inhalation (the $H_2^{15}O$–$^{15}O_2$ protocol), or $^{15}O_2$ inhalation followed by $H_2^{15}O$ injection (or $C^{15}O_2$ inhalation) (the $^{15}O_2$–$H_2^{15}O$ protocol).

MATERIALS AND METHODS

The validity of the present method was first evaluated using the data obtained from a series of *PET* scanning on anesthetized monkeys, in which the global *OEF* values obtained using this approach were compared with those derived using the catheter-based method for measuring the arteriovenous difference (A–V difference) of oxygen contents. Second, image consistency was evaluated by comparing the quantitative values of regional *CBF* and $CMRO_2$ for young normal volunteers derived by the present DBFM and those by the previously proposed DARG methods. Third, the error sensitivity of the present method was evaluated by a simulation study, and was referred to the results for the DARG technique.

Subjects

The subjects consisted of two groups, namely, six normal monkeys of *macaca fascicularris* under anesthesia and seven young normal volunteers. All monkeys were males with a mean body weight of 5.2 ± 0.8 kg and ages ranging from 3 to 4 years. Animals were maintained and handled in accordance with the Human Care and Use of Laboratory Animals guidelines (Rockville, National Institute of Health/Office for Protection from Research Risks, 1996). The study was approved by the local Committee for Laboratory Animal Welfare, National Cardiovascular Center, Osaka, Japan. The protocol also followed the Guidelines for Animal Experimentation of the National Cerebral and Cardiovascular Center, Osaka, Japan.

All normal human subjects were males with a mean age of 25.3 ± 2.4 years and mean body weight of 64.2 ± 6.8 kg. None had symptoms at the time of *PET* examination, or histories of cerebral or other relevant diseases. All subjects gave written informed consent, approved by the ethics committee of the National Cerebral and Cardiovascular Center, Osaka, Japan.

Positron Emission Tomography Experiments (Animal)

Details regarding the primate animal study have been previously reported.[9] Briefly, anesthesia was induced with ketamine (10 mg/kg, intramuscularly) and maintained during the experiment using intravenous propofol (4 mg/kg h) and vecuronium (0.05/mg kg h). Animals were intubated and their respiration was controlled by an anesthetic ventilator (Cato, Drager, Germany). The *PET* scanner used was the ECAT HR (Siemens-CTI, Knoxville, TN, USA), installed in the animal *PET* laboratory of the National Cerebral and Cardiovascular Research Center. Positron emission tomography scanning was performed in 2D mode. After a 900-second transmission scan, a dynamic scan was started following the inhalation of $C^{15}O$. After 10 minutes, a 6-minute dynamic *PET* scan was performed during sequential administration of $^{15}O_2$ (2,200 MBq) and $H_2^{15}O$ (370 MBq) for 3 minutes each. After 10 minutes, another order of scan, namely, $H_2^{15}O$ followed by $^{15}O_2$ administration scan was performed. The administration order, either $H_2^{15}O$–$^{15}O_2$ or $^{15}O_2$–$H_2^{15}O$, was randomized across subjects. Arterial blood was withdrawn continuously from the femoral artery through a catheter (0.6-mm inner diameter) using a syringe pump (Harvard Apparatus, Holliston, MA, USA, model 55-2309) with a withdraw speed of 0.45 mL/min (2.7 mL in total) and the blood radioactivity concentration was measured with a continuous input function monitor system made of GSO scintillation crystals.[12] Arterial and sinus blood samples of 0.2 mL each were drawn simultaneously during each scan. The sinus blood was sampled through a 3-F catheter, which was introduced via the femoral vein to the cerebral sinus using a high-resolution digital X-ray imaging system (GE Medical System, Waukesha, WI, USA). To avoid mixing with venous blood draining from extracranial tissues, the tip of the catheter was carefully placed at the angle of the cerebral sigmoid and transverse sinuses, and its position was confirmed at the conclusion of each *PET* protocol. Their oxygen contents were measured to obtain the global *OEF* ($gOEF_{A\text{–}V}$).[9,13]

In three of the six animals, A–V sampling was performed during the *PET* scan with the $^{15}O_2$–$H_2^{15}O$ protocol at normocapnia ($PaCO_2 \cong 40$ mm Hg) and also while the respiratory rate was sequentially adjusted to achieve hypocapnia ($PaCO_2 < 33$ mm Hg), mild hypercapnia ($45 < PaCO_2 < 50$ mm Hg), and deep hypercapnia ($PaCO_2 > 50$ mm Hg). At least 30 minutes were allotted to reach a steady-state P_aCO_2, after which the $^{15}O_2$–$H_2^{15}O$ *PET* scan was initiated.

Positron Emission Tomography Experiments (Young Normal Volunteer)

Young normal volunteers were studied at the Radiology Department of the National Cerebral and Cardiovascular Research Center. Young, healthy volunteer subjects were scanned with an ECAT 47 scanner (Siemens-CTI). The scanning was carried out in 2D mode. After a transmission scan, a static scan was started at 2 minutes after the end of 4-minute inhalation of 3,000 MBq of $C^{15}O$. After a pause of 10 minutes to permit radioactive decay, two sets of dynamic scans of 540 and 510 seconds were carried out, first during sequential inhalation of $C^{15}O_2$ (3,000 MBq) and $^{15}O_2$ (4,500 MBq), and second an inhalation of $^{15}O_2$ (4,500 MBq) followed by intravenous $H_2^{15}O$ (1,100 MBq), respectively. Since the ^{15}O label in $C^{15}O_2$ is rapidly transferred to the water pool in the lung capillary bed,[14] the $C^{15}O_2$ inhalation is considered essentially identical to the intravenous administration of $H_2^{15}O$. Thus, $C^{15}O_2$–$^{15}O_2$ procedure is noted as $H_2^{15}O$ ($C^{15}O_2$)–$^{15}O_2$ protocol in this article.

Arterial blood was continuously drawn from the brachial artery using a catheter (0.5-mm inner diameter) and syringe pump (Harvard Apparatus, model 901) at a speed of 2.0 mL/min during the *PET* scan. The total blood withdrawn was ~30 mL. The blood radioactivity concentration was measured using the GSO input function monitor system.[12]

Data Processing

Dynamic sinogram data were corrected for dead time in each frame and for detector normalization. Tomographic images were reconstructed using the filtered back projection method with 4- and 7-mm Gaussian filtering for monkeys and human subjects, respectively. Attenuation correction was applied using transmission data. Scatter correction was also applied by means of the deconvolution scatter function technique.[15] Reconstructed images, with a matrix size of 128 × 128 × 47 and a voxel size of 1.1 mm × 1.1 mm × 3.4 mm for monkeys and 1.8 mm × 1.8 mm × 3.4 mm for normal human subjects, were transferred to a LINUX computer for further analysis using in-house programs.

Measured arterial blood time–activity curves (TACs) were normalized to become consistent to *PET* images, and were also corrected for dispersion ($\tau = 3$ and 14 seconds for monkeys and humans, respectively).[16] After correcting for delay,[9,17] the blood curves were separated into $^{15}O_2$ (A_O) and $H_2^{15}O$ (A_W) contents as described previously,[18,19] in which the recirculation water, that is, the arterial $H_2^{15}O$ concentration was estimated using manually sampled at nine points and plasma separated activity concentration in the monkey data (details are presented in[18]) and for human data according to a physiological model validated previously with fixing rate constant values as: $k = 0.13$ per minute (production rate of recirculating water), $\Delta t = 20$ seconds (delayed appearance time of recirculating water), $k_w = 0.38$ per minute (forward diffusion rate of recirculating water to body interstitial space) and $p_w = 1.38$ (k_w/k_2, where is k_2 a backward diffusion rate of recirculating water).[18]

Cerebral blood flow, *OEF*, and $CMRO_2$ images as well as those for V_0^O and V_0^W were calculated according to the DBFM formula described above, using reconstructed images and the obtained input functions, and the hemoglobin concentration and saturation of oxygen in the arterial blood. Additionally applying *CBV* data from $C^{15}O$ scan data, *CBF*, *OEF*, and $CMRO_2$ images were also generated using the DARG formula.[9] With DBFM, blood volume was estimated as V_0^O, and the obtained images were converted to *CBV* images as: $CBV = R_{Hct}\ (1-E \cdot F_v)/V_0^O$,[2] where R_{Hct} $(=0.85)$[20] is the peripheral-to-central hematocrit ratio and F_v $(=0.835)$[2] is the effective venous fraction. Images without applying physical decay correction were applied to both DBFM and DARG calculations.

Data Analysis

Regions of interest (ROIs) were drawn on *CBF* images obtained from experiment on monkeys to cover the whole brain. These ROIs were then transferred to the *OEF* and $CMRO_2$ functional images obtained using the DBFM and DARG methods. Quantitative *CBF*, *OEF*, and $CMRO_2$ values generated from DBFM were then compared with those from DARG. Also, *OEF* values obtained from DBFM were compared with those using the A–V sampling technique (OEF_{A-V}) using Bland–Altman plots.

In young normal volunteers, circular ROIs of 6-mm diameter were placed bilaterally on the temporal, frontal, parietal, occipital, and cerebellar, brain stem, caudate, lentiform, thalamus, and central semioval regions, in which attention was made to avoid the region with large *CBV* such as the sinus region. Values for *CBF*, and $CMRO_2$ in the same ROIs were summarized for the cortical gray matter, deep gray matter, cerebellum, and white matter regions, and were compared between DBFM and DARG using Bland–Altman plots.

The *N*-index, which denotes the noise level of parametric images,[21] was obtained from the standard deviation of an image's spatial values, which was derived by subtracting two statistically independent and physiologically equivalent images. This calculation was carried out for *CBF*, *OEF*, and $CMRO_2$ from young normal volunteers using even- and odd-numbered frames, and the obtained *N*-index values were compared between the DARG and DBFM formulae.

All data are presented as mean values ± 1 s.d. Pearson's correlation analysis and linear regression analysis were used to evaluate relationships between the two *CBF* values. $P < 0.05$ was considered statistically significant.

Simulation

Error propagation was evaluated for three error sources, namely: effects of the imperfect delay adjustment,[17] by shifting time in an input function from −4 to 4 seconds, where a positive error represents an overcorrection of delay time; errors in dispersion correction in the input function,[16] by shifting the time constant from −4 to 4 seconds, where a negative error represents undercorrection, as described previously;[9,22] and errors in the assumed blood/tissue partition coefficient (p),[9,10] by varying p from 0.7 to 0.9 mL/g.[10]

The input function for this simulation study was defined based on typical arterial TACs obtained from a human study with water (A_w) and also with oxygen (A_o),[23] and by adding the Aw and Ao with a time lag of 3 minutes between the administrations of $H_2^{15}O$–$^{15}O_2$ and $^{15}O_2$–$H_2^{15}O$. Applying the kinetic formulation of equation (1), tissue TACs were generated for a 'normal' ($CBF = 0.50$ mL per gram per minute, $OEF = 0.4$, and $CBV = 0.04$ mL/g), 'ischemic' ($CBF = 0.30$ mL per gram per minute, $OEF = 0.6$, and $CBV = 0.06$ mL/g), 'hyperperfusion' ($CBF = 0.70$ mL per gram per minute, $OEF = 0.3$, and $CBV = 0.04$ mL/g), and 'diaschisis' ($CBF = 0.20$ mL per gram per minute, $OEF = 0.4$, and $CBV = 0.04$ mL/g) conditions.[9] Values of *CBF*, *OEF*, and $CMRO_2$ were then calculated using the true input function and these TACs, by assuming $p = 0.8$ mL/g. Errors in calculated functional values were then plotted as a function of the percentage differences of the assumed values for delay, dispersion, and the partition coefficient.

Additional simulation was carried out to evaluate errors in the estimation of recirculating $H_2^{15}O$ in the arterial blood. Arterial input functions were generated by changing the rate constant (k) that corresponds to the whole body oxygen metabolism, and the delay (Δt) by ±10%, from the fixed value (i.e., $k = 0.13$ per minute and $\Delta t = 20$ seconds), and regional tissue TACs were calculated according to the equation (1), by assuming a 'normal' condition. Cerebral blood flow and $CMRO_2$ values were calculated according to the procedure mentioned above, and the %errors were estimated.

RESULTS

The present DBFM as well as DARG programs successfully calculated functional images of *CBF*, *OEF*, $CMRO_2$, and *CBV* for *PET* data on both monkeys and young normal volunteers. The computation time for parametric images was ~30 seconds using a standard PC installed with GNU/Linux (fc16.x86_64 64 bit, CUP:Intel Core i7 3.07 GHz, Memory: 16 GB).

Quantitative values for whole brain in monkeys were 0.32 ± 0.11 and 0.27 ± 0.09 mL per gram per minute in *CBF* for DARG and DBFM, respectively, 0.56 ± 0.06 and 0.57 ± 0.06 in *OEF* for DARG and DBFM, respectively, and 0.029 ± 0.004 and 0.026 ± 0.004 ml per gram per minute in $CMRO_2$ for DARG and DBFM, respectively. The *OEF* value by the A–V method was 0.54 ± 0.06. The paired *t*-test did not show any significant differences in these values between DARG and DBFM for either order, that is, $H_2^{15}O$–$^{15}O_2$ and $^{15}O_2$–$H_2^{15}O$ ($P > 0.05$, $n = 6$). Also, there were no significant differences in *OEF* between the *PET* and the A–V methods, for either order ($P > 0.05$, $n = 6$). During normocapnia, the P_aCO_2, P_aO_2, S_aO_2, and hemoglobin values were 38.9 ± 1.4, 119 ± 12 mm Hg, 97.3% ± 1.2%, and 13.6 ± 1.0 g/dL, respectively. All these values were considered within the normal range.

Figure 1 shows the Bland–Altman plot of *OEF* as estimated by the DBFM and the A–V method obtained during P_aCO_2 variation. The regression line obtained was: $OEF = 0.99\ OEF_{A-V}-0.01$ ($r = 0.96$, $P < 0.001$, $n = 12$). The intercept was not significantly different from zero ($P > 0.05$), and the slope of the line was close to unity.

Figure 2 shows the Bland–Altman plots of regional *CBF* and $CMRO_2$ values as estimated by DARG and DBFM for young normal

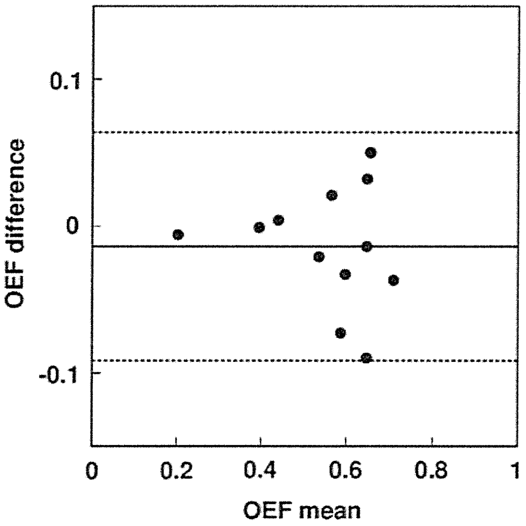

Figure 1. Bland–Altman plots of oxygen extraction fraction (*OEF*) comparing arteriovenous difference (*gOEF*(A–V)) and dual-tracer basis function method (DBFM) (*gOEF*(*PET*)). Solid and broken lines show mean difference and its respective 2 s.d., respectively. Mean ± s.d. values are -0.014 ± 0.038. The regression analysis exhibited a significant positive correlation with a slope close to unity ($y = 0.99\ x + 0.01$, $r = 0.96$, *number of plots* = 12). DBFM was performed with an administration order of O_2–H_2O. *PET*, positron emission tomography.

volunteers. The plots did not show significant differences between DBFM and DARG. Cerebral blood flow or *CMRO*$_2$-dependent changes have not been seen in the plot. Differences in *CBF* were 3.57% ± 6.44% and 3.84% ± 3.42% for the $H_2^{15}O$ ($C^{15}O_2$)–$^{15}O_2$ and $^{15}O_2$–$H_2^{15}O$ protocols, respectively, and those in *CMRO*$_2$ were −2.79% ± 11.2% and −6.68% ± 10.5% in the $H_2^{15}O$ ($C^{15}O_2$)–$^{15}O_2$ and $^{15}O_2$–$H_2^{15}O$ protocols, respectively. Results of the Pearson's regression analysis for *CBF* were: $CBF_{BFM} = 1.07\ CBF_{DARG} - 0.015$ mL per minute per gram ($r = 0.99$, $P < 0.001$) and $CBF_{BFM} = 1.04\ CBF_{DARG} - 0.003$ mL per minute per gram ($r = 0.99$, $P < 0.001$), and those for *CMRO*$_2$ were: $CMRO_{2\ BFM} = 0.93\ CMRO_{2\ DARG} - 0.0022$ mL per minute per gram ($r = 0.93$, $P < 0.001$) and $CMRO_{2\ BFM} = 0.92\ CMRO_{2\ DARG} - 0.0007$ mL per minute per gram ($r = 0.95$, $P < 0.001$) corresponding to the $H_2^{15}O$ ($C^{15}O_2$)–$^{15}O_2$ and $^{15}O_2$–$H_2^{15}O$ protocols, respectively. The mean and s.d. values for *CBF, OEF, CMRO*$_2$, and *CBV* values are summarized in Table 1. The paired *t*-test showed no significant difference in *CBF* between the DBFM and DARG methods for either order. Significant difference was seen in *CMRO*$_2$ and showed smaller values in DBFM with the $^{15}O_2$–$H_2^{15}O$ protocol but not for the $H_2^{15}O$ ($C^{15}O_2$)–$^{15}O_2$ protocol. The *CBV* values by DBFM were essentially within the same order of those obtained by the conventional $C^{15}O$ blood volume scan (noted as DARG in Table 1), but showed significant differences in some regions. No significant difference was seen in V_0^O-derived *CBV* values between the $H_2^{15}O$ ($C^{15}O_2$)–$^{15}O_2$ and $^{15}O_2$–$H_2^{15}O$ protocols.

Figure 3 shows a representative comparison of *CBF, OEF*, and *CMRO*$_2$ images generated by DBFM and DARG from a young normal volunteer. The parametric images generated by DBFM were of comparable quality to those obtained using DARG. The *CBV* images obtained by $C^{15}O$ scanning as well as those calculated from V_0^O and V_0^W for a $^{15}O_2$–$H_2^{15}O$ protocol on a typical young healthy volunteer are compared in Figure 4. *CBV* images from V_0^O showed similar distribution to those produced using the $C^{15}O$ scan, thought the images were noisier. Cerebral blood volume images calculated from V_A^W, on the other hand clearly demonstrate the structure only the internal carotid and middle cerebral arteries, but values are small and in a noise level in other areas.

A comparison of image quality, as defined as the *N*-index divided by the mean value of each of *CBF, OEF*, and *CMRO*$_2$ is given in Figure 5. Values were slightly but significantly greater with DBFM compared with DARG, except *CBF* assessed by the $^{15}O_2$–$H_2^{15}O$ protocol, which did not show significant difference between DBFM and DARG.

Results of the simulation study for the 'normal' condition are shown in Figure 6. Error sensitivity to errors in delay time, the dispersion time constant, and the partition coefficient value were different, but showed the same tendency between the $H_2^{15}O$ ($C^{15}O_2$)–$^{15}O_2$ and $^{15}O_2$–$H_2^{15}O$ protocols for both DARG and DBFM. The magnitude of errors in the calculated functional parameters are within a range of <5% for ± 2 seconds errors in the delay, for ± 2 seconds errors in the dispersion, and for 0.75 to 0.85 mL/g errors in the partition coefficient. The error propergation from each error source to the functional parameters are almost the same in the 'hyperperfusion' condition, but significant magnification was seen in the 'ischemic' condition, and was 1.1 to 1.2 times for *CBF*, 1.6 to 2.0 for *OEF*, and 1.4 to 1.6 for *CMRO*$_2$. For the 'diaschisis' condition, the magnification factors were only 0.1 to 0.5 times for all *CBF, OEF*, and *CMRO*$_2$ parameters. Regarding the errors in the recirculating $H_2^{15}O$ estimation, a change in the oxygen production rate (*k*) by ± 10% resulted in errors of ± 2.5% and 2.1% in *CBF* and *CMRO*$_2$. A change of the delay by ± 10% resulted in errors of 3.0% and 1.2%, respectively.

DISCUSSION

This study demonstrated that the DBFM method developed in this study provided quantitative functional images of *CBF, CMRO*$_2$, and *OEF* from a single, short-duration dynamic *PET* scan with sequential administration protocols of $H_2^{15}O$ ($C^{15}O_2$) and $^{15}O_2$, and $^{15}O_2$ and $H_2^{15}O$ within a short-time interval. Oxygen extraction fraction values obtained by the DBFM method agreed well with those derived by the A–V oxygen difference in the experiment utilizing six normal monkeys (Figure 1). Cerebral blood flow and *CMRO*$_2$ calculated by DBFM also agreed with those by the previously proposed DARG method in young normal volunteers (Figure 2). No significant difference was seen between the DBFM and DARG methods in all functional parameters, except for *CMRO*$_2$ values assessed with the $^{15}O_2$–$H_2^{15}O$ protocol, indicating significantly smaller values with DBFM than DARG. The magnitude of the difference was −6.68% ± 10.5% in average, which is within an acceptable range for practical use. The simulation also demonstrated that the DBFM and DARG methods were similar in terms of the sensitivity to three known error sources of the delay and dispersion, and the uncertainty in the assumed partition coefficient. A previous study[9] demonstrated that calculated functional values were identical between DARG and the three-step autoradiography of Mintun *et al*[2] when the administration interval was longer than 3 minutes in DARG. Dual-tracer basis function method should therefore be able to provide functional values comparable to those of the three-step autoradiography. It should however be noted that the image quality (or the statistical noise) of *CBF, OEF*, and *CMRO*$_2$ images was degraded in DBFM than in DARG as quantitatively evaluated by *N*-Index (Figure 5). This is attributed that four parameters have to be determined in DBFM while only two in DARG. However, difference of *N*-index values was only 10% to 20% in average, and not visible in the calculated parametric images shown in Figure 3.

An important advantage of DBFM over DARG is that the former does not require independent scan of *CBV* using $C^{15}O$ inhalation. This allows shortening the entire scan period. A single dynamic scan for 6 minutes on animal experiments and 9 minutes on young volunteers presented in the present study are significantly shorter than previous protocols. Although additional time is needed for transmission scan and other technical procedures, the entire study period of <15 minutes is probably practically

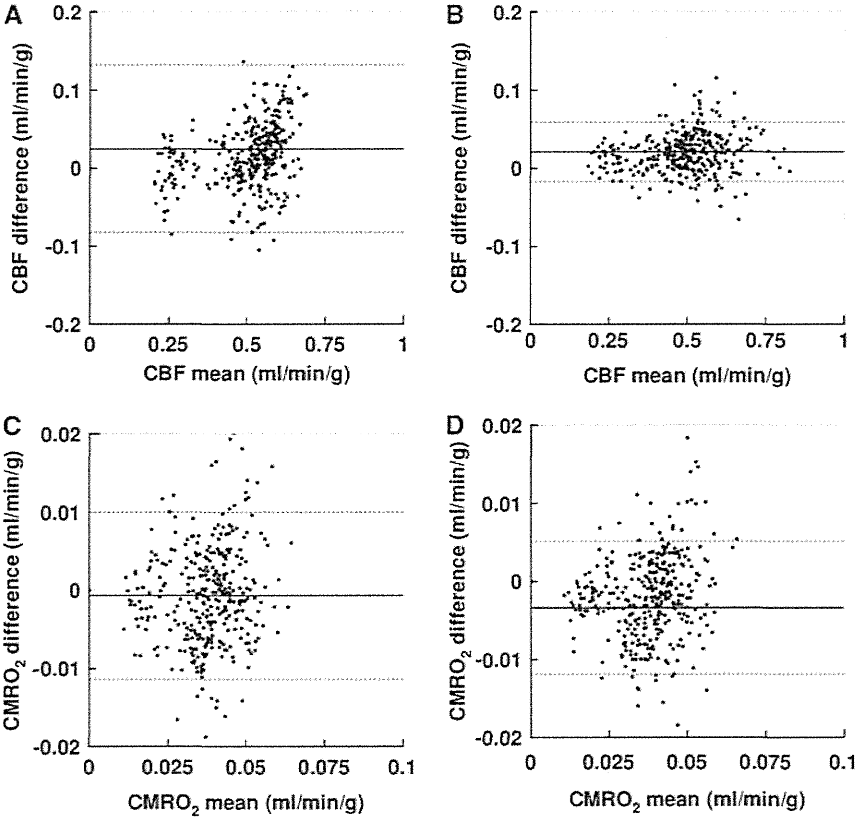

Figure 2. Bland–Altman plots of cerebral blood flow (*CBF*) (upper: **A**, **B**) and metabolic rate of oxygen (*CMRO*$_2$) (lower: **C**, **D**) for $H_2^{15}O$ ($C^{15}O_2$)–$^{15}O_2$ (left: **A**, **C**) and $^{15}O_2$–$H_2^{15}O$ (right: **B**, **D**) protocols comparing dual-tracer autoradiography (DARG) and dual-tracer basis function (DBFM) regional values in young normal volunteers. Solid and broken lines show mean difference and its respective 2 s.d., respectively. Mean ± s.d. values are 0.024 ± 0.030 mL per minute per gram for *CBF* by $H_2^{15}O$ ($C^{15}O_2$)–$^{15}O_2$, 0.021 ± 0.019 mL per minute per gram for *CBF* by $^{15}O_2$–$H_2^{15}O$, -0.000685 ± 0.00536 mL per minute per gram for *CMRO*$_2$ by $H_2^{15}O$ ($C^{15}O_2$)–$^{15}O_2$, and -0.00339 ± 0.00426 mL per minute per gram for *CMRO*$_2$ by $^{15}O_2$–$H_2^{15}O$. Significant difference was observed in *CMRO*$_2$ by $^{15}O_2$–$H_2^{15}O$ in paired *t*-test (**D**), not in others. The regression analysis exhibited a significant positive correlation with a slope close to unity (For *CBF*: $y = 1.07x–0.015$ mL per minute per gram ($r = 0.99$, $P < 0.001$) and $y = 1.04x–0.003$ mL per minute per gram ($r = 0.99$, $P < 0.001$) by $C^{15}O_2$–$^{15}O_2$ and $^{15}O_2$–$H_2^{15}O$ protocols, respectively, and for *CMRO*$_2$: $y = 0.93x–0.0022$ mL per minute per gram ($r = 0.93$, $P < 0.001$) and $y = 0.92x–0.0007$ mL per minute per gram ($r = 0.95$, $P < 0.001$) by $C^{15}O_2$–$^{15}O_2$ and $^{15}O_2$–$H_2^{15}O$ protocols, respectively).

possible and feasible. The DBFM technique is similar to Ohta *et al*[24–27] in terms of estimating three parameters of *CBF*, *CMRO*$_2$, and *CBV* from a single session of the scan. The essential difference is that the DBFM stands for the sequential administration of two tracers of $^{15}O_2$ and $H_2^{15}O$ (or $C^{15}O_2$) within a short interval, which contributes to improve the accuracy and statistical stability. Such shortened *PET* scan makes the simultaneous assessment of *CBF* and *CMRO*$_2$ applicable to a number of physiological and/or pharmacological stimulation studies in clinical settings. Two radioactive compounds, however, need to be synthesized within a short interval, with a high level of purity. An automated system, desirably combined with a dedicated cyclotron, would be the need to improve the logistics of the examination, under the concurrent operation of the radioactivity supply and the *PET* scanning.[28,29] Noninvasive determination of the arterial input function without the arterial blood sampling is also a key issue for practical use of this technique.[30] Further evaluations are warranted.

The present DBFM methods avoids the need for assumption of fixed fractionation of arterial- and venous-parts of the blood volume, as well as the fixed peripheral-to-central hematocrit value, which has commonly been made in the previous DARG and other three-step approaches.[31] Systematic errors could have been caused by these assumptions in pathologic tissues, such as ischemia and/or the AVM (arteriovenous malformation). The ischemia could cause vasodilatation, with a possible change in relative fractionation of arterial-to-venous volumes. The AVM is often characterized by increased arterial blood volume, which likely cause changes in the arterial-to-venous volume fractionations and also in the peripheral-to-central hematocrit ratios. Cerebral blood volume-equivalent information of V_0^O and V_A^W, has been determined in DBFM, thus likely avoiding the systematic errors attributed to the possible alterations in those assumptions. Similar values of *CBF* and *CMRO*$_2$ between the $C^{15}O$-based *CBV* correction in DARG and by DBFM methods in young healthy volunteers, on the other hand, empirically supports the validity of such assumptions in normal controls.

By definition, V_0^O and V_A^W estimated from the DBFM are different from *CBV*, and also different from each other. The former contains both the arterial and venous volume, but more weighted with the arterial part. The latter contains only the arterial blood volume. Further studies should be carried out to evaluate the significance of V_0^O and V_A^W parameters, particularly in patient populations.

Interval of the two administration for the two tracers of $H_2^{15}O$ ($C^{15}O_2$)–$^{15}O_2$ and $^{15}O_2$–$H_2^{15}O$ in DBFM was 3 minutes in animal study, and 6 minutes in young normal volunteer studies. The longer interval in the volunteer study was due to the limitation in radio-synthesis procedures. Use of $C^{15}O_2$ rather than $H_2^{15}O$ would have an advantage in clinical studies, because the venous cannulation for $H_2^{15}O$ saline infusion can be avoided, thus making

Table 1. *CBF*, *OEF*, and $CMRO_2$ values in normal human subjects ($n = 7$) in cortical gray matter, deep gray matter, cerebellum, and white matter regions calculated using DARG and DBFM

	DARG		*DBFM*	
	$H_2^{15}O$–$^{15}O_2$	$^{15}O_2$–$H_2^{15}O$ ($C^{15}O_2$)	$H_2^{15}O$–$^{15}O_2$	$^{15}O_2$–$H_2^{15}O$ ($C^{15}O_2$)
CBF (mL per gram per minute)				
Cortical gray	0.530 ± 0.028	0.514 ± 0.064	0.536 ± 0.026	0.519 ± 0.041
Deep gray	0.522 ± 0.033	0.511 ± 0.038	0.522 ± 0.037	0.505 ± 0.035
Cerebellum	0.539 ± 0.040	0.528 ± 0.041	0.573 ± 0.048	0.535 ± 0.040
White matter	0.278 ± 0.042	0.279 ± 0.044	0.275 ± 0.044	0.289 ± 0.039
OEF				
Cortical gray	0.39 ± 0.05	0.41 ± 0.04	0.39 ± 0.06	0.39 ± 0.03
Deep gray	0.43 ± 0.05	0.43 ± 0.05	0.38 ± 0.05	0.40 ± 0.05
Cerebellum	0.39 ± 0.04	0.41 ± 0.07	0.40 ± 0.05	0.41 ± 0.06
White	0.38 ± 0.03	0.40 ± 0.03	0.38 ± 0.06	0.39 ± 0.03
$CMRO_2$ (mL per gram per minute)				
Cortical gray	0.0415 ± 0.0045	0.0420 ± 0.0041	0.0393 ± 0.0043	0.0399 ± 0.0044*
Deep gray	0.0478 ± 0.0070	0.0469 ± 0.0071	0.0450 ± 0.0075	0.0452 ± 0.0063*
Cerebellum	0.0406 ± 0.0039	0.0435 ± 0.0038	0.0447 ± 0.0039	0.0428 ± 0.0028*
White	0.0207 ± 0.0041	0.0212 ± 0.0036	0.0201 ± 0.0040	0.0208 ± 0.0044
CBV (g/mL)				
Cortical gray	0.0444 ± 0.0088		0.0410 ± 0.0078	0.0574 ± 0.0102*
Deep gray	0.0496 ± 0.0102		0.0444 ± 0.0113	0.0628 ± 0.0110*
Cerebellum	0.0644 ± 0.0038		0.0303 ± 0.0102*	0.0502 ± 0.0079*
White	0.0188 ± 0.0044		0.0224 ± 0.0080*	0.0336 ± 0.0038*

CBF, cerebral blood flow; *CBV*, cerebral blood volume; $CMRO_2$, metabolic rate of oxygen; DARG, dual-tracer autoradiography; DBFM, dual-tracer basis function method; *OEF*, oxygen extraction fraction.
$n = 7$; values are presented as mean ± s.d.; *significant difference ($P < 0.05$) between DARG and DBFM; *CBF* by the DBFM method was calculated from V_0^{O} images as $CBV = R_{Hct}\,(1 - E \cdot F_v)/V_0^{O}$.

the safety control easier. An alternative protocol of inhaling two radioactive gases, namely $^{15}O_2$–$C^{15}O_2$ could be method of choice. The inhalation protocol, however, requires a sophisticated system that enables the stable administration.

One limiting factor of eliminating the additional $C^{15}O$ scan in DBFM is that the calculated *CBF*, *OEF*, and $CMRO_2$ images have enhanced statistical noise. Systematic errors could also be enhanced, if errors in the delay and dispersion of the arterial input function occurring in the catheter tube and connectors etc are not adequately compensated. It should also be noted that the blood volume-equivalent images (V_0^{O}) indicated a large level of statistical noise (Figure 4). Optimization of image reconstruction procedures is required to minimize the enhancement of the statistical noise. Improvement of electronics in the *PET* device for shorter coincidence time window and smaller dead-time count losses are also essential for better quality of images.

Another limitation of the technique is the need for the accurate determination of the arterial input function, as is for other techniques using ^{15}O-labeled compounds. Recent improvements in the spatial resolution and counting rate performance allows the noninvasive determination of the arterial whole-blood input function from the carotid-artery TAC,[30] from which contribution of metabolized $H_2^{15}O$ TAC may be compensated by means of the physiological model.[18] However, an essential technique is needed to ensure the correction for the partial volume effect. Reconstruction of the input function from tissue TACs would also be an alternative. Mathematical formulation with minimal number of parameters that describe the shape of the input function could contribute to provide better accuracy as has been demonstrated in a recent work.[32] Further systematic studies are to be carried out.

The present study was carried out in 2D mode, although the *PET* scanner has ability of 3D acquisition. The reason for this was because we intended to minimize the amount of scatter and the random coincidence rates, attributed to the radioactive gas in the face mask system. The recent *PET* scanner can provide only 3D acquisition. Thus, extensive works are needed to improve the accuracy of the scatter correction method. It is also important to reduce the coincidence time window for reducing the random coincidence counting rate, and to minimize the dead-time count losses. These should be achieved not only by the improvement of the *PET* device, but also by the geometrical optimization of the face mask system including the radioactivity gas transportation.

The *OEF* values of 0.57 ± 0.06 observed in monkeys are higher than those in human. The anesthetic agent of propofol was shown to reduce both *CBF* and $CMRO_2$ with similar magnitude, thus resulting in unchanged *OEF* in young adults.[33] Altman *et al*[34] obtained *OEF* values of 0.53 ± 0.13 using the arterio-sinus blood sampling technique, which is close to the values obtained in this study. It was also shown that *OEF*s measured using the steady-state *PET* technique ranged from 0.42 to 0.58 in normal tissues of anesthetized monkeys,[34–39] which are within the agreement with this study. Cerebral blood flow values ranged from 27 to 37 mL 100 per gram per minute, and $CMRO_2$ from 2.4 to 3.4 mL 100 per gram per minute,[34–39] are also consistent with the results from the present study.

Two administration orders of the two tracers are fixed in healthy young volunteer studies, at first $H_2^{15}O$ ($C^{15}O_2$)–$^{15}O_2$ and then $^{15}O_2$–$H_2^{15}O$, because of the need for a dose calibration each time before $C^{15}O_2$ or $^{15}O_2$ gas supply, after $H_2^{15}O$ saline is produced. This is a source of errors attributed to systemic physiological effect like fatigue or habituation in patients. However, no essential difference was observed between the two protocols in the DBFM method.

A range of *CBF* and the step of basis functions should be carefully selected for the accurate and precise estimation of functional parameters, as has been discussed for neuroreceptor studies.[40,41] The range for *CBF* was set from 0 to 2 mL per minute per gram, with the step value of 0.1 mL per minute per gram in the present computation, which have been confirmed to interpret the human data presented in this work. For the set of solutions in the present formula, we found no other local minimums in the residual sum of squares, for the physiologically acceptable range for *CBF* (0 to 2 mL per minute per gram), *OEF* (0 to 1) and *CBV* (0 to 1 mL/g).

Optimization of administration doses and their ratios of two tracers of $^{15}O_2$ and $H_2^{15}O$ ($C^{15}O_2$) would be a subject of further investigation. Several factors should be taken into account, including the contribution of the residual tracer from the first administration into the second tracer contribution, random counting rate, and dead-time count losses. These are likely dependent on the physical performance of a *PET* device, and therefore need to be investigated for *PET* device-specific manner. The present study, however, demonstrated that the almost equal administration dose could yield stable results.

In conclusion, quantitative *CBF*, *OEF*, and $CMRO_2$ could be calculated using the DBFM method from a single *PET* scan

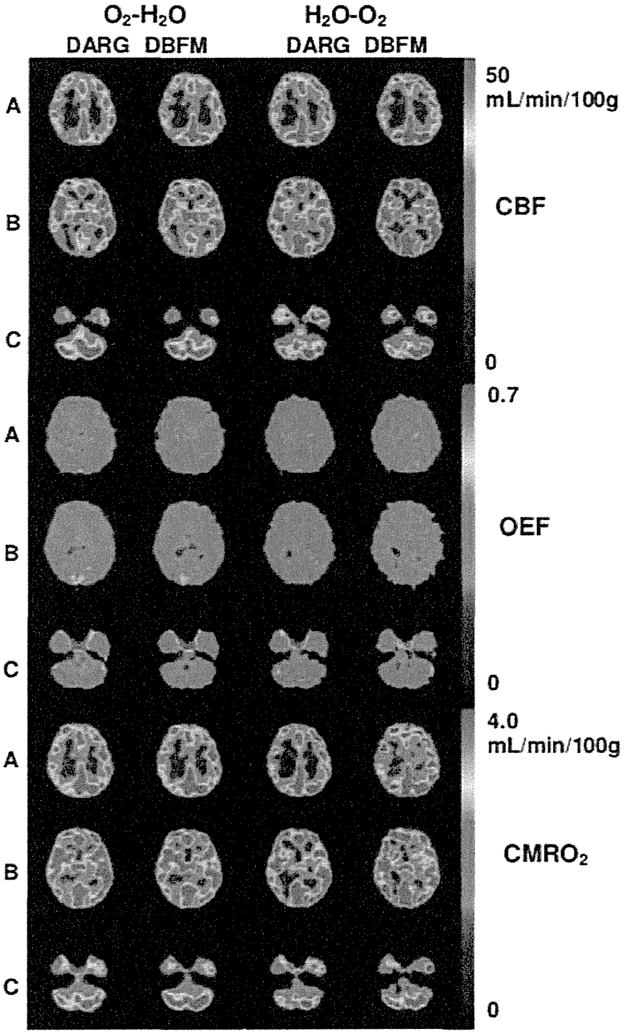

Figure 3. Representative view of cerebral blood flow (*CBF*), oxygen extraction fraction (*OEF*), and metabolic rate of oxygen ($CMRO_2$) images for a normal subject using dual-tracer autoradiography (DARG) and dual-tracer basis function (DBFM) techniques with H_2O–O_2 and O_2–H_2O modes. Axial images are sectioned at (A) parietal level, (B) basal ganglia level, and (C) cerebellar level.

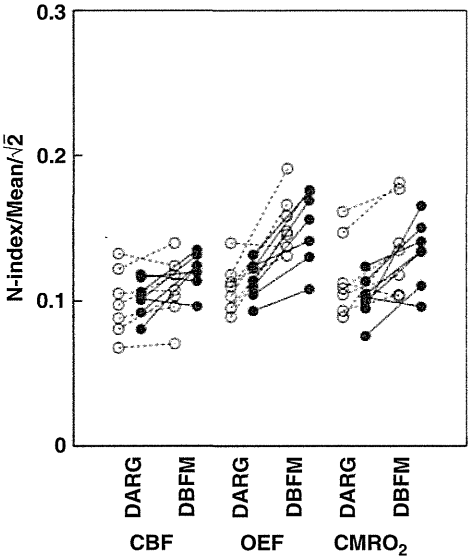

Figure 5. Comparison of noise levels between dual-tracer autoradiography (DARG) and dual-tracer basis function (DBFM) for cerebral blood flow (*CBF*), oxygen extraction fraction (*OEF*), and metabolic rate of oxygen ($CMRO_2$) images by means of *N*-index. White and black circles correspond to values from the $H_2^{15}O$ ($C^{15}O_2$)–O_2 and $^{15}O_2$–$H_2^{15}O$ protocols, respectively. The paired *t*-test shows significant differences in all functional parameters for both protocols between DARG and DBFM except *CBF* by the $^{15}O_2$–$H_2^{15}O$ protocol.

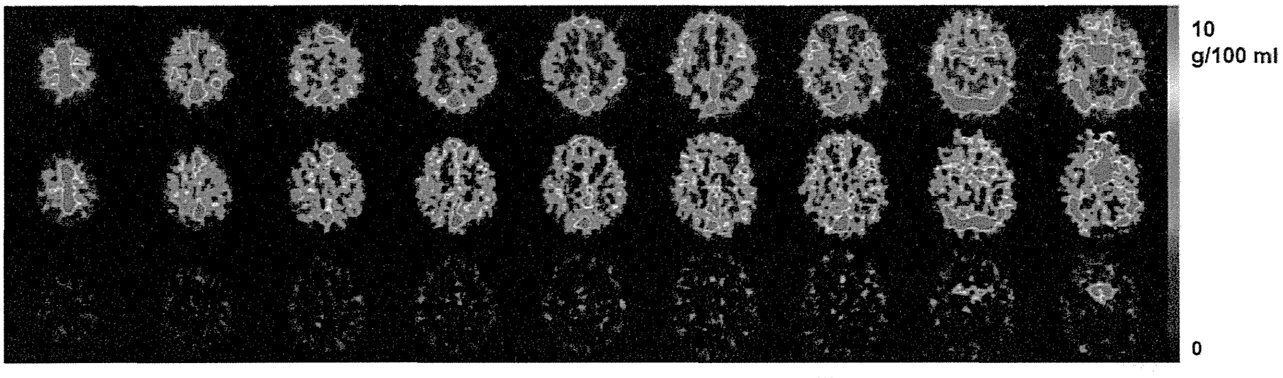

Figure 4. Representative view of cerebral blood volume (*CBV*) (upper and middle) and V_A^W (lower) images in a normal subject, derived by CO scan (upper) and dual-tracer basis function (DBFM) (O_2–H_2O) (middle and lower) methods.